Title
System Response of an Interlayered Deposit with Spatially Preferential Liquefaction Manifestations

Journal
Journal of Geotechnical and Geoenvironmental Engineering, 147(12)

ISSN
1090-0241

Authors
Bassal, Patrick C
Boulanger, Ross W

Publication Date
2021-12-01

DOI
10.1061/(asce)gt.1943-5606.0002684

Peer reviewed

System Response of an Interlayered Deposit with Spatially Preferential Liquefaction Manifestations

Patrick C. Bassal, P.E., S.M.ASCE[1], and Ross W. Boulanger, Ph.D., P.E., F.ASCE[2]

[1]Corresponding author: Graduate Student Researcher, Dept. of Civil and Environmental Engineering, Univ. of California, Davis, CA 95616. ORCID: https://orcid.org/0000-0003-4153-2460. Email: pcbassal@ucdavis.edu.

[2]Professor, Dept. of Civil and Environmental Engineering, Univ. of California, Davis, CA 95616.

ABSTRACT

The Canterbury Earthquake Sequence produced a spatial pattern of liquefaction-induced surface ejecta at an open field along Palinurus Road in Christchurch, New Zealand, that would not be expected based on simplified liquefaction evaluation procedures. Half the site discharged sand boils and the other half did not. Two-dimensional fully-coupled nonlinear dynamic analyses (NDAs) are performed to examine why simplified one-dimensional liquefaction vulnerability indices (LVIs) over-estimated liquefaction manifestations at this site for the 2010 Darfield and 2011 Christchurch earthquakes and did not distinguish between areas with and without surface ejecta. The NDAs use the PM4Sand and PM4Silt constitutive models for sand-like and clay-like portions of the subsurface, respectively, within the FLAC finite difference program. Material parameters are obtained from in-situ geophysical and cone penetration test (CPT) data. A sensitivity study is performed to assess the influence of: (1) representative soil property selections and the use of a CPT inverse filtering procedure to correct for thin-layer and transition zone effects, (2) ground motions developed by two distinct methods (i.e., recordings and physics-based simulations), and (3) model assumptions affecting diffusion during reconsolidation. Ground deformations and flow patterns during and after ground shaking are examined. The results provide insights on how stratigraphic details and other factors can affect the system response and dictate the degree and extent of liquefaction surface manifestations.

Authors' (accepted) copy. JGGE 2021, 147(12):05021013, 10.1061/(ASCE)GT.1943-5606.0002684.

INTRODUCTION

Numerous case history studies (e.g., Chu et al. 2006, Maurer et al. 2014, van Ballegooy et al. 2014, Beyzaei et al. 2018, Cubrinovski et al. 2018, Boulanger et al. 2019) have shown that simplified liquefaction analysis methods can systematically over-estimate the degree and extent of liquefaction surface manifestations, such as sand boils or ground deformations, in specific geologic settings or site conditions. The simplified liquefaction analysis methods examined include a number of one-dimensional (1D) liquefaction vulnerability indices (LVIs) that generally involve depth-weighted integration of predicted strains or factors of safety against liquefaction triggering (as obtained from a stress-based liquefaction triggering analysis) using data from individual borings or cone penetration test (CPT) soundings. Several of these past studies have shown 1D LVIs tend to over-estimate liquefaction effects for deposits where the sedimentary stratigraphy includes interbedded or alternating beds of sands, silts, and clays.

Several factors may contribute to a tendency for over-estimating liquefaction effects in deposits with interbedded or alternating beds of sands, silts, and clays (Boulanger et al. 2016). These include limitations in: (1) site characterization tools and methods, (2) liquefaction triggering or deformation correlations, and (3) analysis approaches and neglected mechanisms. The first set of limitations includes challenges in characterizing thin layers, transition zones, graded bedding, lateral discontinuities, and partial saturation near the water table. The second set includes the uncertainties and biases associated with correlations for cyclic resistance ratio (CRR), and shear and volumetric strains, which are not well-constrained for intermediate soils (e.g., low-plasticity silty sands, clayey sands, or sandy silts) and do not typically account for the effects of age, stress-strain history, cementation, and anisotropy. The third set includes difficulties in addressing spatial variability, pore pressure diffusion, deformation geometries, and the dynamic response. The over-estimation bias of 1D LVIs for these types of deposits is likely due to a combination of the above limitations, depending on the available data, and intricacies of the stratigraphy and soil characteristics for each deposit. By better accounting for several of these limitations, nonlinear dynamic analyses (NDAs) can provide an improved basis, relative to LVIs, for interpreting case histories, as demonstrated by Cubrinovski et al. (2018), Hutabarat and Bray (2019), and Boulanger et al. (2019). NDAs can account for site-specific ground motions and realistic cyclic stress-strain responses; all of which are neglected by LVIs. When performed with a two or three-dimensional (2D or 3D) model, NDAs can additionally account for spatially variable subsurface profiles, pore pressure diffusion, and ground deformation patterns.

This paper describes a 2D NDA study of a site located along Palinurus Road in Christchurch, New Zealand, where: (1) the soil profile includes laterally continuous and discontinuous layers of sands and clayey silts, (2) surficial manifestations of liquefaction (i.e., sand boils) exhibited a preferential spatial pattern, and (3) 1D LVIs were shown by Yost et al. (2019) to over-estimate liquefaction manifestations during the 2010 Darfield and 2011 Christchurch earthquakes. Preliminary NDA results for this case study were presented by Bassal et al. (2020), which showed that accurate modeling of the dynamic response and pore pressure diffusion patterns (mechanisms neglected by 1D LVIs) was necessary to explain the post-earthquake observations. This current work refines the previous study with more detailed examination of how the spatial and temporal responses during and after the 2010 Darfield and 2011 Christchurch earthquakes are influenced by the input ground motions and the NDA model assumptions that affect excess pore water pressure diffusion. The site performance, subsurface conditions, and results of updated 1D LVI analyses are described first. The NDA procedures, constitutive model calibrations, and input ground motions are then described. The NDAs are performed using FLAC (Itasca 2019) with the user defined constitutive models PM4Sand and PM4Silt. Detailed NDA results are presented for a baseline set of parameters, followed by results of parametric studies examining sensitivity to representative property selections and different modeling assumptions. The NDA results are used to evaluate how the dynamic response, ground distortion, and pore pressure diffusion patterns are influenced by details of the subsurface stratigraphy and how such patterns may relate to different liquefaction manifestations across this site during these earthquakes. Insights on system response mechanisms provided by the NDA results are shown to be generally robust despite the uncertainties and limitations in the analysis results and field observations. Implications of these results for informing the interpretation of liquefaction case histories and using NDAs and LVIs in practice are discussed.

PALINURUS ROAD SITE

The 2010-2011 Canterbury Earthquake Sequence (CES) produced a series of strong earthquakes that affected the Canterbury region of New Zealand between September 2010 and December 2011. The CES resulted in well-documented and widespread liquefaction damage throughout the city and adjoining suburbs of Christchurch. Fault projections (Beavan et al. 2012) of the four most destructive events of the CES are shown in Fig. 1. These events are the 4 September 2010 M_w 7.1 Darfield earthquake, the 22 February 2011 M_w 6.2 Christchurch earthquake, the 13 June 2011 M_w 5.3 and M_w 6.0 earthquakes, and the 23 December 2011 M_w 5.8 and M_w 5.9 earthquakes (these events are hereafter labeled as *Sep2010*, *Feb2011, Jun2011, and Dec2011*). Also mapped is the Riccarton High School Strong Motion Station (RHSC SMS), and the location of the Palinurus Road site (-43.5512°, 172.6885°).

The Palinurus Road site is an approximately 90 m by 160 m rectangular and level grass field in the Woolston suburb of Christchurch. The site exhibited little to no evidence of liquefaction during the *Sep2010* and *Dec2011* events, but produced several moderate sand boils during the *Feb2011* and *June2011* events. As depicted in the aerial photograph of Fig. 2, the sand boil ejecta extents were primarily limited to the northeast portion of the site (*NE;* above the dashed line of Fig. 2) during the *Feb2011* event. A similar spatial extent of liquefaction was observed following the *June2011* event. Practically no sand boils emanated on the southwest portion (*SW;* below the dashed line of Fig. 2) during any of the events.

Estimates of the moment magnitude (M_W), rupture distance (R_{rup}), peak ground acceleration (PGA), and observed performance of the Palinurus Road site in the aforementioned four CES events is summarized in Table 1. The PGA was determined based on contours from Bradley & Hughes (2012a, 2012b) for all events except *Feb2011*, for which an interpreted 20% reduction was applied to minimize the influence of high frequency dilation “spikes” recorded at nearby SMS sites that also liquefied (Wotherspoon et al. 2015; Upadhyaya et al. 2019). Although some uncertainty in the actual ground motions at this site is expected, the contour maps and interpreted reduction for the PGA provide reasonable estimates for the LVI analyses that will be presented herein. The observed land damage was assessed based on satellite images depicting the aerial spread of liquefaction ejecta following each event (CGD 2012), and classified based on simplified categories presented by Tonkin & Taylor (2015) ["none to minor" indicates no signs of ejecta, "minor to moderate" indicates < 25% of site covered with ejecta, and "moderate to severe" indicates > 25% of site covered with ejecta]. These land damage classifications are further confirmed by on-the-ground road and property inspections near the site following the *Feb2011 and June2011* events (CGD 2013). The aerial LiDAR surveys performed after the *Feb2011* event do not provide reliable estimates of liquefaction-induced settlements because the vertical accuracy of ±0.15 m in the pre-earthquake surveys (CGD 2014a) encompasses the expected range of settlement. Some ejecta observed following the *June2011* and *Dec2011* events is likely "leftover" from previous events, and thus the reported land damage category is based on an interpretation of "new" or additional ejecta following each event.

The geologic structure of the Christchurch area is highly complex due to its tectonic environment, exposure to pre-Holocene glaciation cycles, and location near the mouth of Pegasus Bay (Begg et al. 2015). Quaternary sedimentary units within the Canterbury basin typically extend to depths of at least 200 m below sea level, and are composed of alternating bands of glacial deposits (i.e., primarily gravels with varying amounts of finer sediments; Riccarton Gravel is the most recent of these deposits), and interglacial deposits (i.e., primarily variable layers of sands, silts, and clays). The current interglacial (i.e., Holocene) sediments are in part comprised of the Christchurch formation (i.e., primarily sands and silts), created by early marine transgressions and ongoing embayment infilling of shallow marine, estuarine, and swamp deposits. The Springston formation (i.e., fluvial silts, sands, and gravels) constitutes the remainder of the Holocene sediments placed by alluvial deposition. The Palinurus Road site is situated about 400 m to the northeast of the meandering Heathcote River, 1100 m to the west of the Heathcote-Avon estuary, and is bounded by a small (~ 4 m wide) stream at its northeast edge. As such, the site is located at an intricate junction of fluvial, estuarine, and swamp deposits, which likely explains the observed stratigraphic heterogeneity and presents difficulty in ascertaining the Holocene soils as Christchurch or Springston formation.

The Palinurus Road site plan shown in Fig. 2 depicts the aerial locations of available site investigation data obtained from the New Zealand Geotechnical Database (NZGD 2019). The site plan includes eight CPTs (5462 to 5469) pushed to refusal and two sonic boreholes (BHs 6000 and 6001) that were conducted in April 2012 as part of a geotechnical investigation considering potential sites for a proposed sewer pump station. Between 2015 and 2016, three additional CPTs (62759, 62760, and 62761), a seismic CPT (SCPT 57360), an additional sonic borehole (BH 57235), and a direct-push crosshole test (DPCH) were completed as part of a regional liquefaction study. The three additional CPTs were pushed to a maximum depth of 16 m, and are the only available information at the *NE* side of the site.

The subsurface profile presented in Fig. 3 shows the nearest BH and CPT data along the cross-section line depicted in Fig. 2. The cone tip resistances normalized by atmospheric pressure (q_{tN}) are presented as measured and after correction for thin-layers and transition zones using the inverse filtering procedure of Boulanger and DeJong (2018) with baseline input parameters. The diagram of BH 57235 in Fig. 3 displays the unified soil classification system (USCS) index, plasticity index (PI), and fines content (FC; percent by soil mass passing a 0.075 mm sieve) with depth.

The subsurface at Palinurus Road is interpreted to have four primary Holocene soil strata (i.e., A, B, C, D) above Riccarton Gravel as shown in Fig. 3. Several of these strata have been divided into subgroups based on variations in engineering properties. The ~3 m thick surface stratum A, is primarily composed of reworked surficial material, with non-plastic silts atop loose silty sands. This is underlain by stratum B, which typically extends to a depth of ~17 m, and is composed of loose to medium dense clean sands with occasional thin (< 10 cm) and very thin (< 1 cm) silt and organic interbeds. At the *SW*, stratum B is interrupted by stratum C at depths of ~6 to 9 m. The upper portion of stratum C (i.e., C1 in subsequent analyses) is composed of soft to firm silt of moderate plasticity, with an estimated overconsolidation ratio (OCR) of 2 to 4, and occasional thin silty sand interbeds. This overlies very loose to loose silty sand with thinly interbedded clayey silt (i.e., C2). Stratum C was not observed in the three CPTs at the *NE* half of the site. Stratum D underlies B, and is composed of a ~1-m thick layer (i.e., D1) of soft clayey silt of moderate plasticity, with an interpreted OCR of 1 to 1.3, often overlying loose to medium dense silty sand lenses with occasional silt interbeds to a depth of ~20.5 m (i.e., D2). D2 silty sands were encountered in six of the nine CPTs that were pushed to refusal. Stratum D may belong to the Avonside Member of the Christchurch formation; a distinct unit, prevalent throughout eastern Christchurch (Begg et al. 2015). Finally, stratum E represents the upper few meters of the Riccarton Gravel formation, comprised of very dense silty and sandy gravel.

The groundwater table depth is estimated at 1.2 m below the ground surface during the earthquakes, based on nearby piezometer readings (CGD 2014b). The compression wave velocity (V_P) was observed to be about 1,500 m/s just below a depth of 1.2 m, which suggests the soil is fully saturated (Yost et al. 2019). Partial saturation is therefore not expected to affect the cyclic resistance of soils below the water table. The drillers of BH 6000 and 6001 reported inflowing artesian pressures at depths of 24 m, with a head of ~1 m above the ground surface. These conditions indicate the existence of high excess pore pressures (Δu) within the Riccarton Gravel, likely obstructed from dissipating upwards by the relatively continuous and low permeability stratum D1.

LIQUEFACTION VULNERABILITY INDEX ANALYSIS

One-dimensional LVI analyses by Yost et al. (2019), performed with the stress-based liquefaction triggering procedure of Boulanger and Idriss (2014), for this site generally indicated an over-estimation of liquefaction manifestations for the 1D LVI metrics considered and for both the *Sep2010* and *Feb2011* earthquakes. These LVI analyses were repeated using the same assumptions made by Yost et al. (2019), with the following exceptions: (1) integration was extended to a depth of 16 m rather than being limited to 10 m, (2) a reduced PGA (as given in Table 1) was considered for the *Feb2011* event, (3) inverse filtering of the CPT data for transition and thin layer effects was evaluated, and (4) site-specific calibration for the fines content correction factor (C_{FC}) per Boulanger and Idriss (2014) of 0.21 for measured and 0.27 for inverse filtered CPT data determined based on correlating laser diffraction readings of the fines content (i.e., percent particles by mass less than 0.075 mm) in samples from BH 57235 with readings from adjacent SCPT 57360. For brevity, results are presented for only the Liquefaction Severity Number (LSN; van Ballegooy et al. 2014) and the 1-D vertical reconsolidation settlement ($S_{v\text{-}1D}$; Zhang et al. 2002) indices, together with the cumulative liquefied thickness (CLT). The liquefaction potential index (LPI; Iwasaki et al. 1978) and Ishihara-inspired index (LPI_{ISH}; Maurer et al. 2015) were also determined to result in generally similar predictions.

The results of the LVI analysis are summarized in Table 2 listing the range and mean values obtained for the CPTs in the *SW* and *NE* areas. A predicted damage category of expected liquefaction manifestations is also indicated based on LSN thresholds proposed by McLaughlin (2017), where LSN < 16 correlates to "none to marginal," 16 ≤ LSN < 26 correlates to "moderate," and LSN ≥ 26 correlates to "severe." The overall conclusions for the *Sep2010* and *Feb2011* earthquakes are essentially the same as those by Yost et al. (2019). The LVI values obtained for the *NE* CPTs (i.e., near sand boils) are similar to those for the *SW* CPTs (i.e., away from sand boils) for each earthquake, and thus the LVIs provide no delineation between the areas that did and did not have surface ejecta. For example, the mean LSN for the *SW* versus *NE* areas for the *Feb2011* earthquake were 36 versus 39 when using the measured CPT data and essentially equal at 26 when using inverse filtered CPT data. Overall, the LSN and $S_{v\text{-}1D}$ in Table 2 are generally consistent in showing: (1) an over-prediction of liquefaction manifestations for these earthquakes, (2) a slight reduction in the degree of over-prediction when using inverse filtered CPT data, and (3) a lack of differentiation between the areas that did and did not have surface ejecta.

NONLINEAR DYNAMIC ANALYSIS METHODOLOGY

Numerical Model

Two-dimensional NDAs of the *SW-NE* trending cross section (Fig. 3) were performed using the finite-difference program FLAC 8.1 (Itasca 2019) and the user-defined constitutive models PM4Sand (Version 3.1; Ziotopoulou and Boulanger 2016, Boulanger and Ziotopoulou 2017) and PM4Silt (Version 1; Boulanger and Ziotopoulou 2018, 2019). The idealized profile is depicted on the 100-m-long central portion of the plane-strain mesh shown in Fig. 4. Stratum B is divided into B1 and B2 to account for slight property differences with depth. Strata C and D are modeled as having a fine-grained layer (i.e., C1 and D1) overlying a sand layer (i.e., C2 and D2) to reflect the typical apportioning of these interbedded layers. The full model mesh is 200 m long by 25 m tall, and is made up of 10,000 elements, each 1.0 m long by 0.5 m tall. Sensitivity analyses showed that the dynamic response of the 100-m long central portion of the mesh is insensitive to the lateral boundary conditions for this mesh length, although the mesh length does influence pore pressure dissipation after the end of shaking as discussed later. Stress conditions were initialized prior to dynamic loading with elastic moduli that produce a coefficient of earth pressure at-rest (K_o) of 0.5 for all soil strata. The water table was initialized with a static phreatic surface at 1.2 m below the ground surface.

The dry density, porosity, vertical hydraulic conductivity (k_V), horizontal to vertical hydraulic conductivity ratios (k_H/k_V), and soil models used in the dynamic analyses are listed in Table 3. The primary set of analysis models assumed isotropic permeability for all strata (i.e., $k_H/k_V = 1$), whereas other analysis models used the listed k_H/k_V ratios to evaluate the effects of anisotropic permeability. Stratum E was modeled as an elastic material with a Poisson's ratio of 0.33; the elastic shear modulus was set to 70% of the small strain shear modulus corresponding to a shear wave velocity of 400 m/s, estimated for this strata based on surface wave (MASW) measurements at nearby sites (Wotherspoon et al. 2015). Rayleigh damping of 0.5% at a frequency of 1 Hz was used in the analyses.

Boundary conditions were selected to approximate free-field conditions during earthquake excitation. A compliant (quiet) base was used, with the outcrop input motion applied as a horizontal stress-time history. The left and right boundaries of the model (50 m away from the boundaries shown in Fig. 4) were attached together; other analyses using "free field" side boundary conditions (absorbing boundaries) confirmed that the system responses in the 100 m long central portion were generally insensitive to the choice of boundary condition. The pore pressure boundary conditions were freed (i.e., impermeable) at the sides of the model and fixed (i.e., allowed to flow outside the model) at the base and top of the model. Thus, the dissipation of excess pore pressures (Δu) generated during shaking is accompanied by net seepage flows into the soils above the static phreatic surface or downward through the model base.

Groundwater flow was modeled both during and following earthquake excitation. Seepage rates during dynamic shaking were relatively small, such that the FLAC solution process was controlled by dynamic time step requirements (i.e., including ground water flow did not significantly slow the solution process).

For simulating post-shaking pore pressure diffusion, an alternative solution process is required for efficiency because of the long time frames involved. For the present analyses, the post-shaking reconsolidation process was sped up by scaling all k_V (with k_H/k_V held constant) by a factor of 100 at the end of strong shaking, which effectively scales the post-shaking time by a factor of 1/100. In addition, the k_V of the surficial stratum A was further increased by a factor of 10 to 1.0E-04 m/s (e.g., equivalent to k_V of stratum B) to approximately account for the effects of cracking and the formation of sand boil pipes which cannot be explicitly simulated using FLAC. The influence of this permeability reduction is evaluated as part of the sensitivity studies later described. The PostShake option of the PM4Sand and PM4Silt constitutive models was activated at the end of strong shaking to more reasonably simulate volumetric reconsolidation strains after shaking. Analysis results are compared for the time when at least 80% of Δu has dissipated in all vertical soil columns above D1 and within the central 60 m of the model mesh, which was sufficient time for the majority of surface settlements to have developed (the influence of mesh dimensions and consolidation time are later discussed).

Calibration of Constitutive Models

The PM4Sand and PM4Silt constitutive models were calibrated for four sets of representative values for the normalized clean sand corrected tip resistance (q_{c1Ncs}) for the sand strata and the undrained shear strength ratio (s_u/σ'_{vc}) for the fine-grained soil strata, respectively. The representative value sets were determined as: (1) 33rd percentile from measured CPT data (*33Meas*), (2) 50th percentile from measured CPT data (*50Meas*), (3) 33rd percentile from inverse filtered CPT data (*33IF*), and (4) 50th percentile from inverse filtered CPT data (*50IF*). Inverse filtering was performed per Boulanger & DeJong (2018) with baseline filter parameters. For each stratum, 33rd and 50th percentile values for q_{c1Ncs} or s_u/σ'_{vc} were obtained based on all CPTs at the site. The 33rd to 50th percentile range is expected to encompass reasonably unbiased estimates of expected responses based on the findings of Montgomery and Boulanger (2016) for NDAs involving an evaluation of post-liquefaction reconsolidation settlements.

Fig. 5 depicts cumulative distribution functions (CDFs) of q_{c1Ncs} for all sand strata (i.e., A, B1, B2, C2, D2). The q_{c1Ncs} values were calculated using the relationships of Boulanger and Idriss (2014) with a site-specific C_{FC} from all CPT readings with $I_c \leq 2.6$. The faded lines depict the CDFs for data from individual CPTs, while the bold line represents the CDF for the data from all CPTs combined. For stratum B, the CDFs for all CPT data in the upper B1 and lower B2 substrata show relatively small differences between these two substrata. Inverse filtering of the CPT data results in slightly greater q_{c1Ncs} values and increased CDF variability among individual CPTs for each stratum. As most evident in strata C2 and D2, the difference in q_{c1Ncs} between the measured and inverse filtered data tends to increase at larger q_{c1Ncs} values. The stratum B CDFs display the least variation among individual CPTs, as expected since (1) it is a thicker stratum (i.e., more sample points are expected to better constrain the shape of the distribution), and (2) it is consistently represented in all CPTs with only occasional interbeds.

Fig. 6 depicts CDFs of the undrained shear strength ratio (s_u/σ'_{vc}) for the fine-grained soil strata (i.e., C1, D1). In the absence of vane shear testing or site-specific laboratory data, the undrained shear strength ratio (s_u/σ'_{vc}) was calculated based on an assumed cone bearing factor (N_{kt}) of 15 for all soil with $I_c > 2.6$. Only selective depth intervals of fine-grained soils were targeted within the C and D strata, to further minimize the influence of thin interbeds and transition zones. The individual and combined CPT CDFs depict s_u/σ'_{vc} typically decreasing due to inverse filtering. As with the sand strata, the individual CPTs show greater variability with inverse filtering.

The calibrated PM4Sand parameters for the four sets of representative properties are presented in Table 4. The unitless shear modulus coefficient (G_o) was determined based on the V_s and effective stresses at the middle of each stratum, as approximated from the DPCH and SCPT data. The apparent relative densities (D_R) were derived from the applicable representative q_{c1Ncs} for each stratum using the relationship in Boulanger and Idriss (2014). The contraction rate parameter (h_{po}) was chosen based on an iterative adjustment to obtain a peak shear strain of 3% with a target normalized cyclic resistance ratio ($CRR_{M7.5,1atm}$) in 15 uniform stress cycles of simulated undrained direct simple shear (DSS) loading. The $CRR_{M7.5,1atm}$

target value was obtained based on the q_{c1Ncs} relationship by Boulanger and Idriss (2014). Default values were used for all secondary PM4Sand parameters.

The calibrated PM4Silt parameters are presented in Table 5. The G_o was determined based on the V_s and effective stresses at the middle of each stratum, as approximated from the DPCH and SCPT data. The undrained strength ratio at critical state under earthquake loading ($s_{u,cs,eq}/\sigma'_{vc}$) for each stratum is based on a 25% increase for strain rate effects and the assumption of relatively modest post-peak strain softening for the range of strains that develop in these simulations. The h_{po} parameter was chosen based on an iterative adjustment to obtain a reasonable slope of cyclic resistance against the number of uniform loading cycles to cause a 3% peak shear strain under simulated DSS loading; e.g., cyclic stresses of 0.7 times $s_{u,eq}$ reached the failure criterion in about 15-20 cycles. The simulated undrained cyclic loading response with a default shear modulus parameter (h_o) resulted in shear modulus reduction and equivalent damping behavior similar to the empirical relationships of Darendeli (2001) for strata C1 and D1. Default values were used for all other secondary PM4Silt parameters.

The differences in the calibrated constitutive responses are illustrated in Fig. 7 showing the cyclic stress ratio versus number of uniform cycles to 3% peak γ (N) for the B2 sand (Fig. 7a) and D1 clayey silt (Fig. 7b) for the *33Meas*, *50Meas*, *33IF*, and *50IF* property sets. These results illustrate that using the inverse filtered CPT data generally produced greater strengths for the sands and lower strengths for the clays and silts. These property sets cover a range of conceivable model parameterizations for the different interlayered soils encountered at the site, thereby indirectly encompassing model parameter variations that could have been derived by varying other components of the liquefaction analysis procedures (e.g., overburden stress corrections; liquefaction triggering correlations; fines content corrections).

Development of Ground Motions

Input motions for each of the *Sep2010* and *Feb2011* events were developed by two approaches: (1) deconvolution of a nearby recording over a "stiff" profile with scaling for site-to-source path effects, per the approach used by Ntritsos et al. (2018), (2) physics-based ground motion simulations by Razafindrakoto et al. (2016). Two horizontal components, labeled H1 for north-south and H2 for east-west trending motions, were considered separately for each ground motion set of each event. Fig. 8 depicts acceleration time-histories and associated response spectra for the eight horizontal input motions considered.

The first approach used to develop input ground motions involved a modification of the outcropping motions recorded ~10 km away at the RHSC SMS (GeoNet n.d.). This station, located in an area that did not experience liquefaction during the CES, was chosen to avoid strong nonlinear soil site effects that could invalidate deconvolution procedures. The recordings at that station were first deconvolved to the Riccarton Gravel stratum using the 1D equivalent-linear site response program Strata (Kottke et al. 2018), following the guidance and recommended procedure detailed in Markham et al. (2016). To account for site-to-source path effects, the resulting motions were scaled with a least-squares fit to the mean empirical ground motion model (GMM) by Bradley (2013) between spectral periods of 0.5 to 1.0 seconds. This range of periods spans the initial fundamental period of the modeled soil profile (above Riccarton Gravel) under initial conditions ($T_{n,i}$), to $2T_{n,i}$, to account for period lengthening that may occur during the earthquake. The GMM and associated standard deviation bands were developed for each event, assuming a shear wave velocity over 30 m (Vs_{30}) of 400 m/s (representing the profile at depths greater than those being explicitly modeled), and fault parameter estimates from Beavan et al. (2012). The modified RHSC input motions are hereafter labeled as RHSC*. The applied scaling factors were 1.0, 1.25, 1.8, and 2.6 for the *Sep2010* H1 and H2, and *Feb2011* H1 and H2 RHSC* motions, respectively.

The second approach involved obtaining ground motions from 3D physics-based simulations, which can account for some of the complexity of the Canterbury basin and source-to-site path effects. Ground motion simulations (hereafter labeled as GMSs) have been shown to typically predict ground motions with comparable bias and uncertainty as empirical GMMs for Christchurch sites during the CES, provided local site effects are properly considered (de la Torre et al. 2020). For the present study, GMSs by Razafindrakoto et al. (2016), which are based on the methodology of Graves and Pitarka (2010), were obtained from the *SeisFinder* database (QuakeCore n.d.), at a location within 200 m from Palinurus Road for the *Sep2010* and *Feb2011* events. These GMSs use a finite difference scheme to propagate low frequency (< 1 Hz) waves through a 3D viscoelastic model with a grid spacing of 100 m and a minimum shear wave velocity (V_S) of 500 m/s. High frequency (> 1 Hz) waves are modeled using a semi-empirical approach with a stochastic source radiation pattern and simplified 1D wave propagation. The motions obtained from *Seisfinder* include a pre-applied V_{S30}-based site amplification function by Campbell and Bozorgnia (2014), with truncation at short and long periods as recommended by Graves and Pitarka (2010), to account for local site conditions. To allow for proper input of the GMSs within Riccarton Gravel, the amplification function was removed in the frequency domain for each simulation, using an iterative procedure recommended by C. de la Torre (personal communications). The resulting GMSs did not require further deconvolution due to the model V_S cap at 500 m/s, which is an adequate assumption for an elastic halfspace boundary within Riccarton Gravel. A vertical GMS motion was also obtained for the *Feb2011* event and was included as part of a sensitivity analysis as later discussed.

Differences in the intensity, frequency content, and duration of the input ground motions are depicted in Fig. 8. For the *Feb2011* event, the GMS motions have a shorter duration and different frequency content than the RHSC* motions. In particular, the GMS motions begin with a long period (1 to 2 s) pulse, preeminent in the fault normal (i.e., H1) direction, which may be expected due to near-fault directivity effects. Recordings at nearby PRPC (~2.8 km N of Palinurus Road) and CCCC (~3.5 km NW) SMSs each exhibit similar short durations and at least one long period pulse, albeit with a slightly greater distance from the fault and location atop different profiles that liquefied (Wotherspoon et al. 2015). The RHSC* motions may have unrepresentative longer durations due to the far-field distance of the recording station, which may have been influenced by surface waves and path-dependent dispersion. The GMS motions may therefore provide more realistic interpretations of the actual motions at Palinurus Road for the *Feb2011* event. For the *Sep2010* event, although the duration between the motions from each approach is similar (i.e., as expected, since both approaches consider similar path effects relative to the source location), the GMS motions have consistently higher spectral accelerations than the GMM at all periods between 0.4 and 3 s. Simulations for the *Sep2010* event generally over-estimate both recordings and the GMM (Razafindrakoto et al. 2016), which may in part be due to complications in modeling the multi-fault rupture of this event (de la Torre et al. 2020). Thus, the RHSC* motions may better represent the motions experienced at Palinurus Road during the *Sep2010* event. Nonetheless, it is of interest to examine how the dissimilarities of the two sets of motions, both derived through reasonable approaches, affect the computed response at Palinurus Road for each event.

DYNAMIC SIMULATION RESULTS

Results are presented for NDAs examining the effects of using the *33Meas*, *50Meas*, *33IF*, and *50IF* property sets and the four different input motions for the *Feb2011* and *Sep2010* events, followed by sensitivity analyses that include the effects of parameters that influence pore pressure diffusion. Dynamic responses for the *Feb2011* event are described in greater detail for three cases to illustrate some key features of the responses when there are significant liquefaction effects. Dynamic responses for the *Sep2010* event are described in less detail because many of the analysis cases did not exhibit significant liquefaction effects, consistent with observations at the site following this event.

Dynamic Response during February 2011 Event with 33rd Percentile Measured Properties

The dynamic response of the model with *33Meas* properties subjected to the GMS-H1 input motion for the *Feb2011* event is depicted in Fig. 9 showing time histories of the cyclic stress ratio (CSR), engineering shear strain (γ), and excess pore pressure ratio (r_u) at six depths on both the southwest (*SW,* x=19.5 m) and northeast (*NE,* x=89.5 m) sides of the site. Also shown is the calculated CSR within stratum E, at x=50 m, which was modeled as linear elastic. The CSR is computed as the ratio of the cyclic horizontal shear stress to initial vertical consolidation stress (σ'_{vc}). The r_u is computed as one minus the ratio of the current to initial vertical effective stress (i.e., $1 - \sigma'_v/\sigma'_{vc}$), which is preferred over using $\Delta u/\sigma'_{vc}$ for system level analyses wherein the total vertical stress may fluctuate; the two definitions are equivalent if the total vertical stress does not change during loading. For presentation purposes, liquefaction of an element is considered to have been triggered wherever r_u becomes greater than or equal to 95%.

Several observations can be made from the CSR, γ, and r_u plots of Fig. 9. A significant aspect of the GMS-H1 motion is that it contains a large full-cycle velocity pulse, which causes CSR to reach a peak at

5.2 s. This pulse causes large shear strains within the soft D1 clayey silt stratum, reaching a maximum γ of 19% (note the depicted element responses in D1 at a depth of 17.25 m on the *SW* and *NE* sides reach a slightly lower peak γ of 10% due to their position one row above the D1 row that reaches γ of 19%). During the last half-cycle of the pulse (e.g., 6.3 s), liquefaction is triggered throughout much of the C2 and B2 sands. Following the pulse, several smaller cycles of loading (CSR < 0.2) continue causing significant cyclic variations in shear strain and contribute to slight increases of r_u with time, as observed in the *NE*-7.75 m plots between 7 to 12 s. The r_u steadily increases from 6.5 s until the end of shaking for the shallow *NE*-3.25 and *NE*-6.25 m plots, which is attributed to pore pressure migration from deeper layers that liquefied earlier (a sensitivity analysis confirmed that 20-30% less soil liquefies without flow during shaking). Fig. 9 also shows the dissipation of r_u for 100 minutes after shaking. Pore pressures within the *SW* sand layers underlying the low-permeability C1 silt stratum, are the slowest to dissipate due to their elongated dissipation path around the silt layer.

Contours of the maximum r_u and γ during shaking are shown in Fig. 10. The responses are relatively uniform across the model for depths below 7.5 m, including the extent of liquefaction triggering (i.e., high r_u) across the B2 sand and the peak strain strains across the underlying D1 clayey silt. Along the top 6 m of the profile, there is significantly more liquefaction in the B1 sand at the *NE* as opposed to the *SW* despite these two areas experiencing almost equal CSR time histories (Fig. 9). The more extensive triggering of liquefaction in the B1 sand at the *NE* is attributed to upward seepage (i.e., pore pressure diffusion) from the underlying B2 sand which liquefied earlier. Pore pressure diffusion and seepage from the B2 sand at the *SW* is impeded in the vertical direction by the lower permeability C1 silt, such that upward flow into the overlying B1 sand during strong shaking is greatly reduced in this area. Pore pressure diffusion from the B2 sand at the *SW* is instead controlled by horizontal seepage toward the *NE* until it passes beyond the end of the C1 silt, which takes more time and thus occurs primarily after the end of strong shaking.

The temporal trend of excess pore pressure diffusion and ground water flow following strong shaking indicates that the majority of the outflow occurred on the *NE* side, just beyond the right edge (x=53 m) of the low-permeability C1 stratum. Isochrones of the total outflow volume per area (Q_{VOL}/A) at the phreatic surface are plotted versus the x-position along the model in Fig. 11. The Q_{VOL}/A as defined herein provides a unit length measure of the cumulative pore water volume that drains vertically towards the phreatic surface, normalized by the horizontal area perpendicular to flow. It is calculated along the row of mesh elements just below the phreatic surface and is used to provide a general understanding of the spatial distribution of the total flow quantity at the ground surface. In reality, this value is likely affected by several details in the crust that might affect the exact flow path and formation of ejecta at the surface, and so it is only treated as a relative indicator among the models considered in this report. Associated isochrones of the vertical settlement (Δy) relative to stratum D1 during reconsolidation are also shown in Fig. 11; settlements relative to the middle of stratum D1 are used for this comparison because the ground water flow during pore pressure diffusion is upward toward the phreatic surface for soils above D1 and downward toward the model base for stratum D2 that underlies D1. At 100 s after shaking, Q_{VOL}/A is approximately equal to Δy along the full width of the model. This synchronicity is expected because the outflows at this time are associated with volumetric strains in the near surface soils (i.e., closest to the drainage boundary), without much influence from flow processes at greater depths. The Δy and Q_{VOL}/A at this time are greater at the *NE* than at the *SW* because there is more extensive shallow liquefaction at the *NE*, which results in greater upward hydraulic gradients and outflow rates. As time progresses, the Δy and Q_{VOL}/A isochrones gradually diverge with $Q_{VOL}/A \geq \Delta y$ to the *NE* and $Q_{VOL}/A < \Delta y$ to the *SW*. The Q_{VOL}/A is greatest just north of the end of the C1 stratum (x between ~50 to 70 m), with the peak "final" Q_{VOL}/A of 20 cm being more than three times the "final" Δy of 6 cm. The Q_{VOL}/A does remain approximately equal to Δy further to the *NE* (e.g., x > 100 m) where pore pressure diffusion is not significantly influenced by lateral flows. Conversely, the Q_{VOL}/A remains small above the C1 stratum on the *SW* side (x < 40 m), with the final Q_{VOL}/A of 1 cm being a small fraction of the final Δy of 3-4 cm.

The results in Fig. 11 correspond to a common final time of 6.6 hours, which is when 80% of Δu has dissipated in all soil columns above D1 and within the central 60 m of the model. The post-earthquake Δy

time histories in Fig. 12 depict how the displacements at times beyond 80% reconsolidation (i.e., beyond the dashed line at 6.6 hours) level out towards a constant value for soil columns located at the *SW* (x = 19.5 m) and *NE* sides (x = 89.5 m). Allowing reconsolidation to progress from 80% to about 95% (i.e., 6.6 to 14 hours) in all columns causes about 10 to 20% more settlement at only the *SW* side, increases the outflow at only the center of the site by 10 to 20% (i.e., the peak outflow is slightly more pronounced), and more than doubles the computational times to approximately one week. The peak outflows are more strongly dependent on the horizontal length of the model because that controls the consolidating soil volume. The field stratigraphy is not known outside the area of site explorations, such that the reconsolidation analyses primarily serve to illustrate relative values and patterns in surface outflows.

The results in Fig. 11 illustrate that reconsolidation of the soils beneath the lower permeability C1 silt stratum on the *SW* side is accommodated by ground water flowing laterally toward the *NE* side, where it can more easily escape to the ground surface. Ground water fluxes of less than 1 cm on the *SW* side appear consistent with the absence of sand boils in this area, and ground water fluxes of up to 20 cm on the *NE* side appear consistent with observations of sand boils in that area. The delayed development of outflow is also consistent with the documented time span of sand boil formations; the spouting of ejecta often begins after shaking and continues for tens of minutes (Housner 1958, Ambraseys and Sarma 1969). The computed settlements of 3-4 cm to the *SW* and 6 cm to the *NE* are reasonably consistent with the absence of visible ground cracking, given that settlements of less than ~10 cm would be difficult to detect visually in a grass field unless they varied sharply over short distances.

Dynamic Response during February 2011 Event – Effect of Properties

The effect of the alternative representative property sets (Tables 4 and 5) on dynamic response was evaluated using the GMS-H1 input motion for the *Feb2011* event. As depicted in Fig. 7a and 7b, the *33Meas*, *50Meas*, *33IF*, and *50IF* property sets represent variable cyclic responses for which clay-like soils may be weaker or stronger than sand-like soils for a given set. For instance, the cyclic strengths for the D1 clayey silt is greater than for the B2 sand when using the *33Meas* property set for all cycles greater than N=3, but smaller when using the *33IF* property set for all cycles.

The dynamic response for *33IF* properties is depicted by the time history, contour, and isochrone plots in Figs. 13, 14, and 15, respectively. Referring to the time histories of CSR, γ, and r_u in Fig. 13, the initial large pulse in the input motion causes yielding and large shear strains (i.e., > 10%) in the D1 clayey silt, which limits the magnitude of the cyclic stresses transmitted to the overlying strata. The CSR in D1 at *NE*-17.25 m and *SE*-17.25 m tend to cap at ~0.25, consistent with the cyclic strength shown in Fig. 7b. The transmitted stresses produce CSR in the overlying strata that are insufficient to trigger liquefaction or significant shear strains except within the C2 loose sand at *SE*-7.75 m. The CSR time series in Fig. 13 are significantly weaker than those obtained for the *33Meas* property set (Fig. 9), with the reductions in CSR attributed primarily to the D1 stratum being significantly weaker for the *33IF* property set (Fig. 7b). Comparing the contours of r_u and maximum γ for the *33IF* properties (Fig. 14) and *33Meas* properties (Fig. 10) similarly illustrates how the weaker D1 strength limited large shear strains to the D1 stratum and limited liquefaction triggering to the C2 stratum on the *SE* side.

The isochrones of Q_{VOL}/A and Δy following strong shaking for the *33IF* case (Fig. 15) show the effects of lateral ground water flow during pore pressure diffusion are similar to those for the *33Meas* case (Fig. 11), notwithstanding the less extensive triggering of liquefaction. In this case, the *SW* experiences a larger Δy than the *NE* (i.e., 1 cm versus 0.2 cm) because liquefaction triggering was largely limited to the C2 stratum on the *SW* side. Diffusion of excess pore pressures from the C2 stratum is again dominated by lateral seepage toward the *NE*, leading to the seepage outflow at the phreatic surface (Q_{VOL}/A) being greatest just past the northern edge of the C1 silt stratum. The maximum final Q_{VOL}/A of 5.4 cm is far greater than the Δy of 0.2 cm at this location or the Δy of 1 cm toward the *SW*. These Δy are consistent with the absence of visible surface settlements or ground cracking, whereas the maximum seepage outflow seems sufficient to have produced visible sand or water ejecta in this local area.

Results of the NDAs using the four representative property sets with the GMS-HI input motion for the *Feb2011* event are summarized in the first four rows of Table 6, which lists several metrics of the dynamic response (i.e., maximum γ in D1, CLT at the *SW* and *NE*) and post-earthquake response (i.e., Δy at the *NE* and *SW*, maximum Q_{VOL}/A, reconsolidation time). The response metrics using the *50Meas* properties are similar to those obtained using *33Meas* properties (e.g., Figs. 9-11), with both cases predicting the CLT to be more than 6 m on both the *SW* and *NE* sides, surface settlements of about 3.5 cm to the *SW* and 6 cm to the *NE*, and peak surface outflows of 20-21 cm just north of the C1 stratum. The response metrics using the *50IF* properties are similar to those obtained using *33IF* properties (e.g., Figs. 13-15), with both cases predicting the CLT to be about 1 m to the *SW* and 0 m to the *NE*, surface settlements of about 1 cm to the *SW* and 0.2 cm to the *NE*, and peak surface outflows of 5 cm just north of the C1 stratum. The limited extent of liquefaction triggering for the *50IF* case is attributed to it having the greatest cyclic strengths for the B1 and B2 sand strata (Table 4 and Fig. 7a), whereas the limited extent of liquefaction triggering for the *33IF* case was attributed to it having the weakest cyclic strengths for the D1 stratum (Fig. 7b).

Dynamic Response during February 2011 Event – Effect of Input Motion

The effect of alternative input motions for the *Feb2011* event was evaluated first using the RHSC*-H1 motion with the *33Meas*, *50Meas*, *33IF*, and *50IF* property sets. The metrics of the dynamic response for these four cases are summarized in rows 5 through 8 of Table 6. The relative effect of changing property sets were similar to those obtained using the GMS-H1 motion (rows 1 through 4 of Table 6). The responses for the two motions however do affect certain features of the response that are described for the *33Meas* property set below.

The dynamic response for the RHSC*-H1 motion with the *33Meas* property set is depicted by the time history and contour plots shown in Figs. 16 and 17, respectively. The RHSC*-H1 motion contains several large cycles, though none are as large as the initial pulse of the GMS-H1 motion (Fig. 8). Consequently, the maximum γ in the D1 clayey silt is less than 2% for this motion compared to 19% with the GMS-H1 motion (Table 6). Excess pore pressures in the sand strata generally increase with each cycle of loading leading to liquefaction being triggered in C2 (7.75 m depth) at 6.2 sec, in D2 (18.25 m depth) and the middle portion of B2 (7.75m depth) at ~9 sec, and in B1 (3.25 m depth) and more widely in B2 (5.25 m and 13.25 m depths) at ~12 sec. The effects of liquefaction triggering at different depths and times are evident in the waveform characteristics of the acceleration and CSR time series. The more extensive liquefaction in B2 at the *NE* as compared to the *SW* was likely caused by the early liquefaction triggering in C2, which altered the dynamic response and limited the peak CSR that could be experienced on that side thereafter.

Contours of the maximum r_u and γ during shaking in Fig. 17 show that the B1 and B2 strata have greater volumes of liquefied soil at the *NE* side as opposed to the *SW* side. The greatest γ (5 to 9%) developed in the C2 and D2 silty sands, although significant strains also developed along the bottom of stratum A (~3%) and throughout stratum B2 on the *NE* side (~ 2 to 5%). The overall pattern of strains are consistent with the cyclic behavior and relative densities of each stratum. The isochrones of Q_{VOL}/A and Δy following strong shaking for the RHSC*-H1 motion shown in Fig. 18 are similar to those for the GMS-H1 motion (Fig. 11), except for the Δy being slightly greater to the *NE* (10 cm versus 6 cm). The peak final Q_{VOL}/A is 20-21 cm just north of the edge of the C1 stratum for both motions, which suggests that the C1 stratum would be expected to have similar effects on the likely distribution of surface ejecta despite the differences in the input motions and dynamic site response.

The effects of other variations in input motions were evaluated with the *33Meas* properties, with the results summarized in the last four rows of Table 6. For the *33Meas* properties, the GMS-H1, GMS-H2, RHSC*-H1, and RHSC*-H2 motions produced generally similar values for the CLT (4.5-7.5 m to *SW*, 7-17 m to *NE*), surface settlements (2.7-3.7 cm to *SW*, 4.3-9.7 cm to *NE*), and maximum Q_{VOL}/A (15-21 cm). Responses using the GMS-H1 motion with reversed polarity and the GMS-H1 motion with the vertical component included were both within 10% of the response for the GMS-H1 motion alone.

The GMS and RHSC* alternative input ground motion sets produce differences in the dynamic response but ultimately similar liquefaction effects, which may partially be explained by differences in the ground motion's intensity near the site period and duration (number of effective cycles). These effects have similarly been observed to have a compensating influence on simplified liquefaction triggering when comparing near-fault motions in the strike normal direction (i.e., with larger cyclic stresses but fewer equivalent cycles), with the strike parallel direction (e.g., Green et al. 2008). GMS-H1 in this case is characteristic of a motion with directivity effects and RHSC*-H1 may be likened to a motion without directivity effects. For this site, similar liquefaction effects may also be attributed to a complex interplay between different soil layers and the timing of high intensity cycles, whereby early yielding in some layers have influenced the transmitted CSR to other layers (as also observed by Cubrinovski et al. 2018).

Lateral Variations in Surface Motions and Horizontal Ground Strains

The variation in ground surface motions from the *SW* to *NE* are illustrated by the acceleration time series and response spectra for the *33Meas* properties with the GMS-H1 and RHSC*-H1 motions in Fig. 19. The accelerations at the ground surface for locations to the *SW* and *NE* for the GMS-H1 motion have only slight differences over the full duration of shaking, with both showing significant damping of motions after liquefaction is triggered during the first strong pulse of motion. The response spectra for the surface motions are higher than the base spectrum at low periods up to 0.04 s, are primarily lower between 0.04 to 1.5 s, and are very slightly higher at periods above 1.5 s. Both surface spectra are fairly consistent with one another, except the *SW* motion is slightly lower at all periods below 0.1 s. The accelerations at the ground surface for points to the *SW* and *NE* for the RHSC*-H1 motion also have only slight differences over the full duration of shaking, with the effects of liquefaction triggering evident after about 7 s. The surface time histories for this motion display prominent high frequency "dilation spikes" after the onset of liquefaction. These spikes are attributed to "liquefaction shockwaves" (Kutter and Wilson 1999) associated with the constructive wave interference that can develop if the waves passing through a liquefied soil are strong enough to produce incremental dilation and stiffening (e.g., the transient stiffening phase during cyclic mobility). The response spectra for the surface motions are higher than the base spectrum at low periods up to ~0.07 s, are then lower up to 0.7 s, and are higher at periods above 1.0 s. The *NE* surface spectrum is at least 30% higher than the *SW* at low periods up to 0.3 s, but they are roughly equal at larger periods. The peak surface acceleration for both input motions is slightly smaller on the *SW* side, which may be attributed to the influence of the relatively weaker/looser C1 and C2 strata on this side.

Variations in horizontal ground strains across the site are illustrated by the contours of maximum horizontal extensional and compressive strains (ε_x) in Fig. 20 for the *33Meas* model subjected to the GMS-H1 (Fig. 20a) and RHSC*-H1 (Fig. 20b) motions. The slight differences in the ground motions on the *SW* and *NE* sides of the site, due to the slightly different profiles and differences in liquefaction responses, produce horizontal strains in the near surface soils near the central portion of the site (i.e., around the northern edge of the C1 stratum). These maximum horizontal strains are greater for the RHSC*-H1 motion than for the GMS-H1 motion, which is consistent with greater differences in surface accelerations between the *SW* and *NE* sides (Fig. 19). Additional deformations in the near surface soils can be expected to arise from lateral variability in soil properties (e.g., Montgomery and Boulanger 2016), which is not accounted for in these analyses. The maximum horizontal strains in this area during shaking exceed 0.2% for the RHSC*-H1 motion and for several other of the analysis cases listed in Table 6. The cycling of horizontal extensional and compressive strains in this area may be sufficient to promote surface cracking and facilitate sand boil formation, particularly in combination with the local concentration of seepage outflows.

Sensitivity of Diffusion Behavior to Other Model Variations

Four different model assumptions that influence pore pressure diffusion were examined using the *33Meas* model with the GMS-H1 motion: (1) reduced lateral extent of stratum C, (2) anisotropic permeabilities, (3) decreased crust permeability, and (4) increased crust permeability at locations assigned cracks due to excessive tensional strains. All five models had similar extents of liquefaction triggering and ground surface settlements, with the only significant differences being in the pore pressure dissipation responses. The final distributions of Q_{VOL}/A and Δy are shown in Fig. 21, at the time when at least 80% of Δu has dissipated in all vertical soil columns above D1 and within the central 60 m of the model. The first model variation was reducing the length of stratum C. The 200 m long baseline model drains all Δu beneath a 103 m long stratum C to the *NE*. This assumption implies Δu has no other direction to flow (e.g., no water outlets through low permeability stratum C1; no flow to the *SW* or in the third dimension). To check the sensitivity of this assumption, the model extents were reduced to 160 m and C1 was reduced to 83 m, preserving the center portion of the model with minimal boundary disturbance. This ~20% reduction in the length of C1 resulted in only a ~10% reduction of peak outflow, while preserving the same shape as the baseline Q_{VOL}/A. The second model variation was including anisotropic k_H/k_V values listed in Table 3. This change caused a ~20% reduction in the peak outflow and slightly broadened the Q_{VOL}/A distribution. This result is expected due to a higher k_H causing flow lines to spread further laterally beyond the edge of the C1 stratum before turning toward the surface. The third model variation was decreasing k_V of stratum A by a factor of 10 relative to the base case (i.e., k_V remains constant at $1/10^{th}$ that of the underlying B2). This reduced the peak outflow by ~40%, broadened the Q_{VOL}/A distribution, and reduced *NE* reconsolidation by 1.9 cm. The broader Q_{VOL}/A distribution is attributed to the buildup of Δu below stratum A, which allowed Δu to spread laterally beneath A as it dissipated into A. The settlement at the *NE* side was reduced because the average degree of consolidation at the *NE* side is about 10% less than the base case, even for the same reconsolidation criteria (Fig. 12); these differences in settlement and peak outflows are smaller if the results are compared at closer to 100% consolidation throughout the full profile. The fourth model variation imposed a tenfold increase of k_V for any zone in stratum A with extensional strains greater than 0.05% (this arbitrary threshold value was selected for qualitative insight). This resulted in an irregular Q_{VOL}/A distribution (because the increase in k_V was irregular, as may be expected with the development of irregular crack patterns) and an almost 40% increase in the peak Q_{VOL}/A value. In all cases, the peak Q_{VOL}/A is located near x=55-60 m, just north of the lateral edge of the C1 stratum.

Dynamic Response during September 2010 Event – All Cases

Results of the NDAs using the four property sets with the RHSC*-H1 motion and the *33Meas* property set with the four alternative input motions for the *Sep2010* event are summarized in Table 7. No liquefaction occurred using the *33Meas*, *50Meas*, *33IF*, or *50IF* properties with the RHSC*-H1 motion, and liquefaction was limited to a 0.5-m thick zone on the *SW* side using the *33Meas* properties with the RHSC*-H2 motion. The Δy was less than 1 cm and the maximum Q_{VOL}/A was less than 3 cm for these cases, in congruence with the absence of visible liquefaction manifestations during this event. The responses using the *33Meas* properties with the GMS-H1 and GMS-H2 motions predicted significant CLTs (1.5-7.5 m to *SW*, 4.5-14 m to *NE*), surface settlements (1.6-3.5 cm to *SW*, 2.4-7.3 cm to *NE*), and maximum Q_{VOL}/A (10-22 cm). The input response spectra of the GMS motions produced from the complex multi-fault rupture of this *Sep2010* event have been generally observed to overestimate both the actual recordings and the GMM (Razafindrakoto et al. 2016, de la Torre et al. 2010), and are therefore believed less suited for evaluating dynamic response at this site.

DISCUSSION

The 2D NDA results provide insights and reasonable bounds on the observed patterns of liquefaction manifestation at Palinurus Road for the *Feb2011* and *Sep2010* earthquakes. The parametric studies were generally consistent in indicating that significant liquefaction effects would be expected in the *Feb2011* event and not expected in the *Sep2010* event, although less consistent results were obtained for some combinations of soil properties and input motions. However, all results were consistent in indicating that surface ejecta would be expected to preferentially develop to the *NE* side, even if liquefaction triggering occurred at depth on both the *SW* and *NE* sides. In contrast, the 1D LVI results provide no differentiation to support why surface ejecta was observed to the *NE* side but not to the *SW* side of the site, and generally over-predict the severity of liquefaction manifestations given current empirical thresholds. The advantages of the NDAs relative to the 1D LVIs for this case study are primarily the explicit modeling of dynamic response and 2D pore pressure diffusion and ground distortion patterns. Cubrinovski et al. (2018) demonstrated the importance of accurately accounting for the dynamic system response using 1D NDAs for representative idealized soil profiles, and concluded that the cross-interaction of dynamic effects can be critical for an accurate evaluation of liquefaction effects at sites with various sedimentary structures. The present analyses further enforce those observations. Different facets of an input motion (e.g., near-fault directivity effects, frequency content) may also govern the system response, and these may not be captured by an LVI's consideration of PGA and a magnitude scaling factor alone. Accounting for 2D diffusion and ground distortions was essential to modeling and understanding the spatial distribution of surface expressions of liquefaction. The presence of laterally discontinuous lower-permeability layers can influence the patterns of pore pressure diffusion and consequently alter the distribution of surface manifestations (e.g., sand boils) relative to the actual locations of liquefaction triggering in the subsurface. Case studies performed with 1D LVIs may instead misinterpret liquefaction effects by directly correlating analyses at a single soil column with manifestations directly above it.

The NDA analyses presented in this study show that the system level response was sensitive to modest variations in the properties assigned to the different strata for the input motions considered. Property variations due to different uniform percentile choices (i.e., 33^{rd} and 50^{th}) and alternate CPT processing methods (i.e., measured and inverse filtered) result in significantly different responses due to the relative interaction between layers and the time-dependent distribution of stresses throughout the system. These property sets cover a reasonable range of conceivable model parameterizations, thereby indirectly encompassing cases that could have been derived from other uncertainties in the site characterization and liquefaction analysis procedures (e.g., undrained strength corrections for clays; overburden stress corrections; liquefaction triggering correlations; fines content corrections).

Predicting the occurrence of surface ejecta from NDA results is currently subjective, given the complex mechanics of ejecta pathway formation and soil erosion are not well understood nor accounted for in these types of continuum models. Accordingly, the computed $Q_{VOL/A}$ should be interpreted as illustrating the relative magnitudes and patterns among analyses with similar assumptions, and should not be taken as an accurate predictor of outflows. Hutabarat and Bray (2021) proposed an index for evaluating surface ejecta potential from results of 1D NDAs. The 2D analysis results presented herein suggest that the formation of ejecta pathways can be promoted in areas of differential ground strains, which may be associated with lateral variations in the stratigraphy, soil properties, and extent of liquefaction triggering, along with the influence of stratigraphic variations on pore pressure diffusion patterns.

The potential influence that cyclic softening in strata of soft clays or silts can have on a site's dynamic response was illustrated by NDA cases where the continuous D1 clayey silt stratum was either assigned the lowest scenario strength or was subjected to the stronger initial velocity pulse from the GMS-H1 input motion for the *Feb2011* event. For these cases, cyclic softening in the D1 stratum limited the cyclic stress ratios that developed in the other strata, which greatly reduced the extent of liquefaction triggering. These results reinforce findings by others (e.g., Ghosh et al. 2005) that illustrate the need for adequate characterization of all strata to effectively model highly nonlinear dynamic responses.

NDAs simulate more realistic behavior than LVIs, but nonetheless still have limitations. For instance, they are generally unable to directly simulate some of the physical mechanisms involved with pore pressure dissipation, including void redistribution and the generation of a water film beneath less permeable layers (e.g., Fiegel & Kutter 1994, Boulanger & Truman 1996), changes in permeability during liquefaction, cracking of crust soils due to ground distortions, sedimentation effects during post-liquefaction reconsolidation, and erosion and ground loss during sand boil formation. Such processes may contribute to loosening of sands immediately beneath less permeable layers, such as noted for liquefaction case history sites at Brawley Park in the 1979 Imperial Valley earthquake (Youd 1984) and at the Wildlife Array in the 1987 Superstition Hills earthquake (Holzer et al. 1988), and consistent with the C2 silty sand stratum being looser than the other sand strata at Palinurus Road. Changes in density throughout a sand profile following any one liquefaction event are not expected to be large, but rather to accumulate through several earthquake events, as illustrated by centrifuge model tests with multiple shaking events by Darby et al. (2019). Local pressure gradients from natural permeability contrasts of crust soils may contribute to the precise position and behavior (e.g., jetting, welling up) of sand boils (Housner 1958). Also, the modeled stratigraphy is a simplification dependent on available site data, and may not adequately capture the spatial variability of soil parameters and layer extents. As with LVIs, NDAs are subject to uncertainty from the input parameters, and good practice requires sensitivity analyses to represent a range of expected behavior. The PM4Sand and PM4Silt constitutive models were chosen for their ability to model the cyclic stress-strain behavior of sand-like and clay-like soils. Reasonably similar insights should be expected using other constitutive models with similar capabilities and calibrations (e.g., Montgomery and Abbaszadeh 2017). In spite of these limitations, the NDA results for Palinurus Road reasonably bound the observed liquefaction manifestations and sand boil patterns during these two earthquakes.

CONCLUSION

This paper examined the seismic response of the Palinurus Road site for the *Sep2010* and *Feb2011* earthquakes through a series of 2D NDAs with variations in soil properties, input ground motions, and modeling assumptions. The range of NDA results for each event were generally consistent with, or enveloped, the observed surface manifestations of liquefaction for both events, including the absence of visible liquefaction manifestations for the *Sep2010* event and the development of extensive surface ejecta toward the *NE* side of the site for the *Feb2011* event. Primary observations from these NDAs and companion LVI analyses are summarized as follows.

- The laterally discontinuous lower-permeability C1 stratum on the *SW* side of the site (Figs. 3 and 5) caused pore pressure diffusion from any underlying liquefied zones to be controlled by horizontal seepage toward the *NE* where it can more easily escape to the ground surface. This caused ground water fluxes at the ground surface to be greatly increased (e.g., $Q_{VOL}/A > 20$ cm) in the area north of the end of the C1 stratum and greatly reduced (e.g., < 1 cm) in the *SW* area above the C1 stratum for the *Feb2011* event. These differences in ground water fluxes are consistent with the observed distribution of surface ejecta, and indicate that the absence of surface ejecta on the *SW* side should not suggest that liquefaction was not triggered at depth in these areas.
- Reasonable variations in the soil parameters altered the timing and location of the onset and progression of liquefaction and/or cyclic softening, ultimately influencing the dynamic response. For example, the use of inverse filtered CPT data (to correct for thin layer and transition zone effects) affected responses by reducing estimated strengths for clay-like layers and increasing estimated strengths for sand-like layers. This typically promoted early yielding of the continuous D1 clayey silt stratum, which limited the extent of liquefaction triggering throughout the soil profile.
- The input ground motions developed by two different approaches had significant effects on the dynamic responses and extent of liquefaction triggering. This was primarily due to variations in the frequency content, duration, and consideration of near fault effects (e.g., velocity pulse). However, this did not affect the observation that lower-permeability stratum C1 had a critical effect on pore pressure diffusion patterns and post-earthquake distributions of surface ejecta.

- Lateral variations in the profile from *SW* to *NE* were sufficient to cause dissimilar dynamic responses, leading to a zone of greater horizontal extensional/compressive strains and distortion during shaking, which would increase the potential for ground cracking and ultimately sand boil formation in that area.
- 1D LVIs were limited in their ability to predict or explain the observed field responses at this site. Instead, explicit consideration of the dynamic response and 2D pore water diffusion patterns was important for differentiating between the performance of the *SW* and *NE* sides of the site in terms of the observed post-earthquake sand boil patterns.

This case history illustrates the advantages of NDA methods, relative to simplified 1D LVI methods, wherein the explicit modeling of dynamic response and pore pressure diffusion were essential for approximating the observed responses. These results reinforce findings from other case history studies, including several from the CES (e.g., Cubrinovski et al. 2018), but are also unique in illustrating how surface patterns of ejecta may be shifted relative to the subsurface distribution of liquefied soils by the influence of laterally discontinuous lower-permeability interlayers on the pore pressure diffusion patterns.

DATA AVAILABILITY

Some or all data, models, or code used during the study were provided by third parties. Direct request for geotechnical data and ground motions may be made to the providers indicated in the acknowledgements and requests for software can be made to the providers indicated in the references.

ACKNOWLEDGEMENTS

The authors appreciate the financial support of the National Science Foundation (award CMMI-1635398) and California Department of Water Resources (contract 4600009751) for different aspects of the work presented herein. Any opinions, findings, conclusions, or recommendations expressed herein are those of the authors and do not necessarily represent the views of these organizations. The site characterization data was sourced from the New Zealand Geotechnical Database. Procurement and preparation of the physics-based ground motion simulations benefited greatly from discussions with Chris de la Torre. Examination of this case history benefited from discussions with Brady Cox, Kaleigh Yost, Sjoerd van Ballegooy, Jonathan Bray, Misko Cubrinovski, Ken Stokoe, and Liam Wotherspoon. The analyses benefited from discussions with Jason DeJong, James Dismuke, Nick Paull, Renmin Pretell, and Katerina Ziotopoulou. The authors are grateful for the above support and interactions.

REFERENCES

Ambraseys, N. & Sarma, S. (1969). "Liquefaction of soils induced by earthquakes." Bull. Seismol. Soc. Am.V. 59(2), 651-664.

Bassal, P. C., Boulanger, R. W., Cox, B. R., Yost, K. M., & DeJong, J. T. (2020). "Dynamic analyses of liquefaction at Palinurus Road in the Canterbury Earthquake Sequence." Proc., 40th USSD Annual Meeting and Conference, United States Society on Dams, Denver, CO, 1-17.

Beavan, J., Motagh, M., Fielding, E., Donnelly, N., & Collett, D. (2012). "Fault slip models of the 2010-2011 Canterbury, New Zealand, earthquakes from geodetic data, and observations of post-seismic ground deformation." New Zealand Journal of Geology and Geophysics 55(3).

Begg, J., Jones, K., & Barrell, D. (2015). Geology and geomorphology of urban Christchurch and eastern Canterbury. GNS Science Geological Map 3, Lower Hutt, NZ.

Beyzaei, C.Z., Bray, J.D., van Ballegooy, S., Cubrinovski, M., & Bastin, S. (2018). "Depositional environment effects on observed liquefaction performance in silt swamps during the Canterbury earthquake sequence." Soil Dynamics & Earthquake Engineering, 107: 303-321.

Boulanger, R. W., & DeJong, J. T. (2018). "Inverse filtering procedure to correct cone penetration data for thin-layer and transition effects." Proc., Cone Penetration Testing 2018, Hicks, Pisano, & Peuchen, eds., Delft Univ. of Tech., The Netherlands, 25-44.

Boulanger, R. W., & Idriss, I. M. (2014). "CPT and SPT based liquefaction triggering procedures." Report No. UCD/CGM.-14/01.

Boulanger, R.W., Moug, D.M., Munter, S.K., Price, A.B. & DeJong, J.T. (2016). “Evaluating liquefaction in interbedded sand, silt, and clay deposits using the cone penetrometer.” Proc., 5th International Conference on Geotechnical & Geophysical Site Characterization: Queensland, Australia.

Boulanger, R. W., Munter, S. K., Krage, C. P., & DeJong, J. T. (2019). “Liquefaction evaluation of interbedded soil deposit: Çark Canal in 1999 M7.5 Kocaeli Earthquake.” Journal of Geotechnical & Geoenvironmental Engineering, ASCE, 145(9): 05019007, /10.1061/(ASCE)GT.1943-5606.0002089.

Boulanger, R. W., & Truman, S. P. (1996). “Void redistribution in sand under post-earthquake loading.” Canadian Geotechnical Journal, 33, 829-834.

Boulanger, R. W., & Ziotopoulou, K. (2019). "A constitutive model for clays and plastic silts in plane-strain earthquake engineering applications." Soil Dynamics and Earthquake Engineering, 127(2019): 105832, 10.1016/j.soildyn.2019.105832.

Boulanger, R. W., & Ziotopoulou, K. (2018). “PM4Silt (Version 1): A silt plasticity model for earthquake engineering applications.” Report No. UCD/CGM-18/01, Center for Geotechnical Modeling, Dept. of Civil and Environmental Engrg., University of California, Davis, CA, 108 pp.

Boulanger, R. W., & Ziotopoulou, K. (2017). “PM4Sand (Version 3.1): A sand plasticity model for earthquake engineering applications.” Report No. UCD/CGM-17/01, Center for Geotechnical Modeling, Dept. of Civil and Environmental Engrg., University of California, Davis, CA, 113 pp.

Bradley, B.A. & Hughes, M. (2012a). “Conditional Peak Ground Accelerations in the Canterbury Earthquakes for Conventional Liquefaction Assessment.” Technical Report for the Ministry of Business, Innovation and Employment. 13 April 2012. 22 p.

Bradley, B.A. & Hughes, M. (2012b). “Conditional Peak Ground Accelerations in the Canterbury Earthquakes for Conventional Liquefaction Assessment: Part 2.” Technical Report for the Ministry of Business, Innovation and Employment. 22 December 2012. 19 p.

Bradley, B.A. (2013). “A New Zealand-specific pseudospectral acceleration GMPE for active shallow crustal earthquakes based on foreign models.” Bull. Seismol. Soc. Am. V 103(3). 1801–1822.

Campbell, K. W. and Bozorgnia, Y. (2014). “NGA-West2 Ground Motion Model for the Average Horizontal Component of PGA, PGV, and 5% Damped Linear Acceleration Response Spectra.” Earthquake Spectra 30, 1087–1115.

Canterbury Geotechnical Database (CGD) (2014a). “Verification of LiDAR acquired before and after the Canterbury Earthquake Sequence.” CGD Technical Specification 03.

Canterbury Geotechnical Database (CGD) (2014b). "Event Specific Groundwater Surface Elevations", Map Layer CGD0800 - 10 June 2014. Accessed May 15, 2020. from https://canterburygeotechnicaldatabase.projectorbit.com/.

Canterbury Geotechnical Database (CGD) (2013). "Liquefaction and Lateral Spreading Observations", Map Layer CGD0300 - 22 September 2016. Accessed May 15, 2020. https://canterburygeotechnicaldatabase.projectorbit.com/.

Chu, D. B., Stewart, J. P., Youd, T. L. & Chu, B. L. (2006). "Liquefaction-induced lateral spreading in near-fault regions during the 1999 Chi-Chi, Taiwan Earthquake." J. Geotechnical & Geoenvironmental Engineering, ASCE, 132(12), 1549-1565.

Cubrinovski, M., Rhodes, A., Ntritsos, N., & van Ballegooy, S. (2018). “System response of liquefiable deposits.” Soil Dynamics & Earthquake Engineering, 124, 212-229.

Darby, K. M., Boulanger, R. W., DeJong, J. T., & Bronner, J. D. (2019). “Progressive changes in liquefaction and cone penetration resistance across multiple shaking events in centrifuge tests.” J. of Geotechnical & Geoenvironmental Engineering, ASCE, 140(3): 04018112, 10.1061/(ASCE)GT.1943-5606.0001995.

Darendeli, M. B. (2001). Development of a new family of normalized modulus reduction and material damping curves [Ph. D. dissertation]. University of Texas at Austin.

de la Torre, C. A., Bradley, B. A., & Lee, R. L. (2020). “Modeling nonlinear site effects in physics-based ground motion simulations of the 2010–2011 Canterbury earthquake sequence.” Earthquake Spectra 36(2):856-879.

Fiegel, G. L., & Kutter, B. L. (1994). “Liquefaction mechanism for layered soils.” J. Geotech. Eng. 20(4), 737–755.

GeoNet (n.d.). Geological hazard information for New Zealand: Strong Motion Data Products. Accessed May 1, 2019. ftp://ftp.geonet.org.nz/strong/processed.

Ghosh, B., Klar, A., & Madabhushi, S. P. G. (2005). “Modification of site response in presence of localised soft layer.” J Earthq Eng 9(6):855–876.

Graves, R., & Pitarka, A. (2010). “Broadband ground-motion simulation using a hybrid approach. Bulletin of the Seismological Society of America.” 100: 2095–2123.

Green, R.A., Lee, J., White, T.M., and Baker, J.W. (2008). "The Significance of Near-Fault Effects on Liquefaction," Proc. 14th World Conf. on Earthquake Engineering, Paper No. S26-019.

Holzer, T. L., Youd, T. L., & Bennett, M. J. (1988). “In situ measurement of pore pressure build-up during liquefaction.” 20th Joint Meeting of United States-Japan Panel on Wind and Seismic Effects, Gaithersburg, MD, 1988: 118–130.

Housner, G.W. (1958). “The mechanism of sandblows.” Bull. Seismol. Soc. Am. Vol. 48 pp. 155-161.

Hutabarat, D., & Bray, J. D. (2021). “Effective stress analysis of liquefiable sitess to estimate the severity of sediment ejecta.” J. Geotech. Geoenviron. Eng., ASCE, 147(5): 04021024, 10.1061/(ASCE)GT.1943-5606.0002503.

Itasca (2019). "FLAC, Fast Lagrangian Analysis of Continua, User’s Guide, Version 8.1." Itasca Consulting Group, Inc., Minneapolis, MN.

Iwasaki, T., Tatsuoka, F., Tokida, K., & Yasuda, S. (1978). “A practical method for assessing soil liquefaction potential based on case studies at various sites in Japan.” Proceedings of the 2nd International Conference on Microzonation, Nov 26 – Dec 1, San Francisco, CA, USA.

Kottke, A. R., & Ellen, R. M. (2008). "Technical manual for Strata." Report No.: 2008/10. Pacific Earthquake Engineering Research Center, UC Berkeley.

Kutter, B. L. and Wilson, D. W. (1999). "De-liquefaction shock waves." Proc., 7th US–Japan Workshop on Earthquake Resistant Design of Lifeline Facilities and Countermeasures Against Soil Liquefaction, Tech. Rep. MCEER-99-0019, T. D. O'Rourke, J. P. Bardet, and M. Hamada, eds., State University of New York, Buffalo, N.Y., 295–310.

Markham, C., Bray, J. D., Macedo, J., & Luque, R. (2016). "Evaluating nonlinear effective stress site response analyses using records from the CES." Soil Dynamics & Earthquake Eng. 82, 84–898.

Maurer, B., Green, R., Cubrinovski, M., & Bradley, B. (2014). "Evaluation of the Liquefaction Potential Index for Assessing Liquefaction Hazard in Christchurch, New Zealand." J. of Geotechnical & Geoenvironmental Engineering, ASCE, 140(7): 04014032, A10.1061/(ASCE)GT.1943-5606.0001117.

Maurer, B., Green, R., & Taylor, O. S. (2015). "Moving towards an improved index for assessing liquefaction hazard: Lessons from historical data." Soils and Foundations, JGS, 55(4):778-787.McLaughlin, K. (2017). "Investigation of false-positive liquefaction case history sites in Christchurch, New Zealand." M.S. Thesis. The University of Texas at Austin.

Montgomery, J., and Abbaszadeh, S. (2017). "Comparison of two constitutive models for simulating the effects of liquefaction on embankment dams." Proceedings, 37th Annual USSD Conference, USSD, Denver, CO.

Montgomery, J., & Boulanger, R. W. (2016). "Effects of spatial variability on liquefaction-induced settlement and lateral spreading." J. Geotechnical and Geoenvir. Engineering, ASCE, 04016086, 10.1061/(ASCE)GT.1943-5606.0001584.

New Zealand Geotechnical Database (NZGD) (n.d.). Accessed July 1, 2019. https://www.nzgd.org.nz.

New Zealand Mapping Ltd. (2014). "Christchurch Post-Earthquake 0.1m Urban Aerial Photos (24 February 2011)." LINZ Data Service. Accessed May 1, 2020. https://data.linz.govt.nz/.

Ntritsos, N., Cubrinovski, M., and Rhodes, A. (2018). "Evaluation of liquefaction case histories from the 2010-2011 Canterbury Earthquakes suing advanced effective stress analysis." Geotechnical Earthquake Engineering and Soil Dynamics V, GSP 292, ASCE, 152-164, https://doi.org/10.1061/9780784481479.016.

QGIS (2020). QGIS Geographic Information System. Open Source Geospatial Foundation Project. http://qgis.org.

QuakeCore (2016). Seisfinder. Accessed March 1, 2020. https://quakecoresoft.canterbury.ac.nz/seisfinder/.

Razafindrakoto, H. N. T., Bradley, B. A., & Graves, R. W. (2016). “Broadband ground motion simulation of the 2010-2011 Canterbury earthquake sequence.” Proceedings of the 2016 New Zealand Society of earthquake engineering conference, Christchurch, New Zealand, 1–3 April.

Robertson, P. K. (2010). “Estimating in-situ soil permeability from CPT & CPTu.” Proc., 2nd Int. Symp. on Cone Penetration Testing, Huntington Beach, CA.

Stamen Design (2020). Toner and Terrain: Map Tiles by Stamen Design, under CC BY 3.0. Data by OpenStreetMap, under ODbL. Accessed May 1, 2020. http://maps.stamen.com/.

Tonkin & Taylor Ltd. (2015). “Canterbury Earthquake Sequence: Increased Liquefaction Vulnerability Assessment Methodology.” Chapman Tripp acting on behalf of the Earthquake Commission (EQC), Tonkin & Taylor ref. 52010.140.v1.0.

Upadhyaya, S. (2019). “Influence of corrections to recorded peak ground accelerations due to liquefaction on predicted liquefaction response during the 2010-2011 Canterbury, New Zealand, Earthquake Sequence.” Proc., 13th Australia New Zealand Conference on Geomechanics (13ANZCG).

van Ballegooy, S., Malan, P., Lacrosse, V., Jacka, M.E., Cubrinovski, M., Bray, J. D., O’Rourke, T.D., Crawford, S.A. & Cowan, H. (2014). “Assessment of liquefaction-induced land damage for residential Christchurch.” *Earthquake Spectra*, 30(1), 31-55.

van Ballegooy, S., Wentz, F., & Boulanger R. W. (2015). “Evaluation of a CPT-based liquefaction procedure at regional scale.” *Soil Dynamics and Earthquake Engineering*, 79, 315-334.

Wotherspoon, L.M., Orense, R.P., Bradley, B.A., Cox, B.R., Wood, C.M. & Green, R.A. (2015). “Geotechnical characterization of Christchurch strong motion stations.” Eq.Comm.Rep. Project No. 12/629; v3.

Yost, K. M., Cox, B. R., Wotherspoon, L., Boulanger, R. W., van Ballegooy, S., & Cubrinovski, M. (2019). “In situ investigation of false-positive liquefaction sites in Christchurch, New Zealand: Palinurus Road Case History.” Geo-Congress 2019: Earthquake Engineering and Soil Dynamics, GSP308, ASCE, 436-451.

Youd, T. L. (1984). "Recurrence of Liquefaction at the Same Site." Eighth World Conference on Earthquake Engineering EERI, San Francisco, 231-238.

Zhang, G., Robertson, P.K. & Brachman, R.W.I. (2002). "Estimating liquefaction-induced ground settlements from CPT for level ground." Canadian Geotechnical Journal, 39: 1168-1180.

Ziotopoulou, K., & Boulanger, R. W. (2016). "Plasticity modeling of liquefaction effects under sloping ground and irregular cyclic loading conditions." Soil Dynamics and Earthquake Engineering, 84 (2016), 269-283, 10.1016/j.soildyn.2016.02.013.

Tables and Figures

Table 1. Summary of significant CES events at Palinurus Road.

Event	M_w	R_{rup} (km)	Site PGA (g)[a]	Land damage observation category[b]	
				SW Side	*NE Side*
4 September 2010	7.1	20	0.24	None to minor	None to minor
22 February 2011	6.2	1	0.54	None to minor	Minor to moderate
13 June 2011 (2 events, 80 min. apart)	5.3 & 6.0	1.5	0.29 & 0.42	None to minor	Minor to moderate[c]
23 December 2011 (2 events, 80 min. apart)	5.8 & 5.9	5.5	0.22 & 0.28	None to minor	None to minor[c]

[a] PGA from Bradley & Hughes (2012a, 2012b) contours for all events except *22 February 2011*, for which a 20% reduction was applied to remove the influence of nearby recorded dilation spikes.
[b] Based on categories presented by Tonkin & Taylor (2015).
[c] The noted category represents the authors' interpretation of only the ejecta produced by events of that day.

Table 2. LVI results summary at Palinurus Road during the *Feb2011* and *Sep2010* events.

Event	CPT Processing	Value	*SW Side (9 CPTs)*			*NE side (3 CPTs)*		
			LSN	$S_{V\text{-}1D}$ (cm)	CLT (m)	LSN	$S_{V\text{-}1D}$ (cm)	CLT (m)
Sep2010	Measured	Range	15 - 25	7 - 12	2.7 – 6.1	16- 24	8 - 10	4.7 – 5.2
		Mean	20	9	4.6	19	9	5.0
		Category[a]	Moderate			Moderate		
	Inverse Filtered	Range	11 - 18	5 - 8	2.3 – 3.7	10 - 16	4 - 6	2.3 – 3.4
		Mean	14	7	2.9	13	6	3.0
		Category[a]	None to Marginal			None to Marginal		
Feb2011	Measured	Range	34 - 47	16 - 24	9.3 – 13.9	34 - 40	17 - 19	10.1 – 10.9
		Mean	39	18	10.4	36	18	10.3
		Category[a]	Severe			Severe		
	Inverse Filtered	Range	20 - 35	10 - 17	5.5 – 9.4	24 – 31	11 – 14	6.5 – 7.9
		Mean	26	13	7.0	26	12	7.2
		Category[a]	Severe			Severe		

[a] Predicted damage category based on LSN thresholds presented by McLaughlin (2017).

Table 3. Soil properties and constitutive models assumed for NDA models.

Stratum	Dry Density (kN/m^3)	Porosity	k_V (m/s)[a]	Anisotropic Model k_H/k_V[b]	Soil Model
A	14.7	0.44	1E-05[c]	2	PM4Sand
B1/B2	14.7	0.44	1E-04	2	PM4Sand
C1	14.7	0.44	1E-09	5	PM4Silt
C2	14.7	0.44	1E-05	5	PM4Sand
D1	14.7	0.44	1E-09	5	PM4Silt
D2	14.7	0.44	1E-06	5	PM4Sand
E	17.9	0.46	1E-02	1	Elastic

[a] k_V, estimated from I_c per Robertson (2010).
[b] k_H/k_V for the anisotropic model. Other models assume isotropic permeability for all strata.
[c] At stratum A, k_V of 1E-05 m/s is assumed during shaking for all models. After shaking, k_V is increased to 1E-04 m/s.

Table 4. Dynamic soil properties assumed for PM4Sand strata.

PM4Sand Strata	V_S (m/s)	G_o (-)	*33Meas*			*50Meas*			*33IF*			*50IF*		
			D_R	q_{c1Ncs}	h_{po}	D_R	q_{c1Ncs}	h_{po}	D_R	q_{c1Ncs}	h_{po}	D_R	q_{c1Ncs}	h_{po}
A	115	651	0.53	96	0.32	0.58	106	0.28	0.60	111	0.28	0.65	125	0.30
B1	175	983	0.62	118	0.21	0.66	129	0.23	0.67	132	0.26	0.72	146	0.43
B2	200	839	0.63	119	0.25	0.65	126	0.26	0.71	142	0.42	0.73	149	0.61
C2	165	666	0.54	98	0.30	0.57	105	0.29	0.58	107	0.28	0.62	118	0.28
D2	200	656	0.61	114	0.27	0.64	123	0.29	0.63	120	0.29	0.69	138	0.40

Table 5. Dynamic soil properties assumed for PM4Silt strata.

PM4Silt Strata	V_S (m/s)	G_o (-)	*33Meas*		*50Meas*		*33IF*		*50IF*	
			$s_{u,eq,cs}/\sigma'_{vc}$	h_{po}	$s_{u,eq,cs}/\sigma'_{vc}$	h_{po}	$s_{u,eq,cs}/\sigma'_{vc}$	h_{po}	$s_{u,eq,cs}/\sigma'_{vc}$	h_{po}
C1	165	865	0.74	120	0.95	200	0.54	60	0.80	170
D1	175	498	0.37	40	0.44	60	0.24	10	0.36	30

Table 6. NDA results for *Feb2011* event.

GM source	Comp.	Soil param.	D1 max γ (%)	CLT (m)[a]		Δy (cm)[b]		Max Q_{VOL}/A (cm)	Post-EQ reconsol. time (min)[c]
				SW	*NE*	*SW*	*NE*		
GMS	*H1*	*33Meas*	19.1	7.5	9.5	3.5	6.3	20.2	397
GMS	*H1*	*50Meas*	12.4	8.5	6	3.4	5.6	21.2	415
GMS	*H1*	*33IF*	64.6	1	0	1.0	0.2	5.2	253
GMS	*H1*	*50IF*	23.3	1	0	1.0	0.2	5.1	233
*RHSC**	*H1*	*33Meas*	1.8	6	17	3.7	9.7	21.3	388
*RHSC**	*H1*	*50Meas*	2.2	5	10.5	2.8	4.5	14.3	323
*RHSC**	*H1*	*33IF*	14.6	1.5	0	1.4	0.4	7.7	283
*RHSC**	*H1*	*50IF*	7.4	2	1.5	1.3	1.1	7.0	230
*RHSC**	*H2*	*33Meas*	0.5	4.5	8.5	2.9	4.3	15.1	345
GMS	*H2*	*33Meas*	1.4	5	7	2.7	4.5	15.6	337
GMS	*H1-Rev*	*33Meas*	18.6	8	9	3.5	6.0	20.3	393
GMS	*H1 & V*	*33Meas*	19.8	7.5	8	3.4	5.5	18.5	308

Note: All measurements at the *SW* and *NE* sides are respectively taken at columns along x = 19.5 and 89.5 m.
[a] CLT accumulates 0.5 m thick elements exhibiting a maximum $r_u \geq 95\%$ during shaking.
[b] Post-earthquake reconsolidation monitored until ≥ 80% consolidation as defined in Fig. 12.

Table 7. NDA results for *Sep2010* event.

GM source	Comp.	Soil param.	D1 max γ (%)	CLT (m)[a]		Δy (cm)[b]		Max Q_{VOL}/A (cm)	Post-EQ reconsol. time (min)[c]
				SW	*NE*	*SW*	*NE*		
*RHSC**	*H1*	*33Meas*	0.2	0	0	0.1	0.1	0.8	63
*RHSC**	*H1*	*50Meas*	0.2	0	0	0.1	0.1	0.7	65
*RHSC**	*H1*	*33IF*	0.2	0	0	0.1	0.1	0.7	68
*RHSC**	*H1*	*50IF*	0.2	0	0	0.1	0.1	0.6	68
*RHSC**	*H2*	*33Meas*	0.2	0.5	0	0.6	0.2	2.7	135
GMS	*H1*	*33Meas*	0.9	7	14	3.5	7.3	21.9	475
GMS	*H2*	*33Meas*	0.3	1.5	4.5	1.6	2.4	10.4	328

Note: All measurements at the *SW* and *NE* sides are respectively taken at columns along x = 19.5 and 89.5 m.
[a] CLT accumulates 0.5 m thick elements exhibiting a maximum $r_u \geq 95\%$ during shaking.
[b] Post-earthquake reconsolidation monitored until ≥ 80% consolidation as defined in Fig. 12.

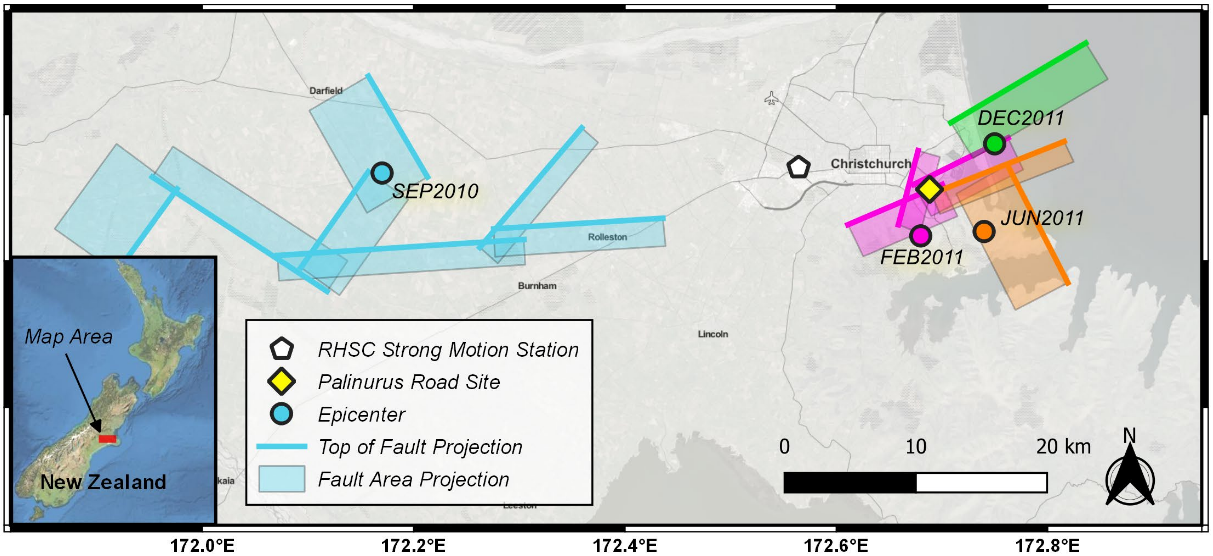

Fig. 1. Fault map depicting significant CES events affecting the Palinurus Road site [base imagery from Stamen Design (2020); made with QGIS].

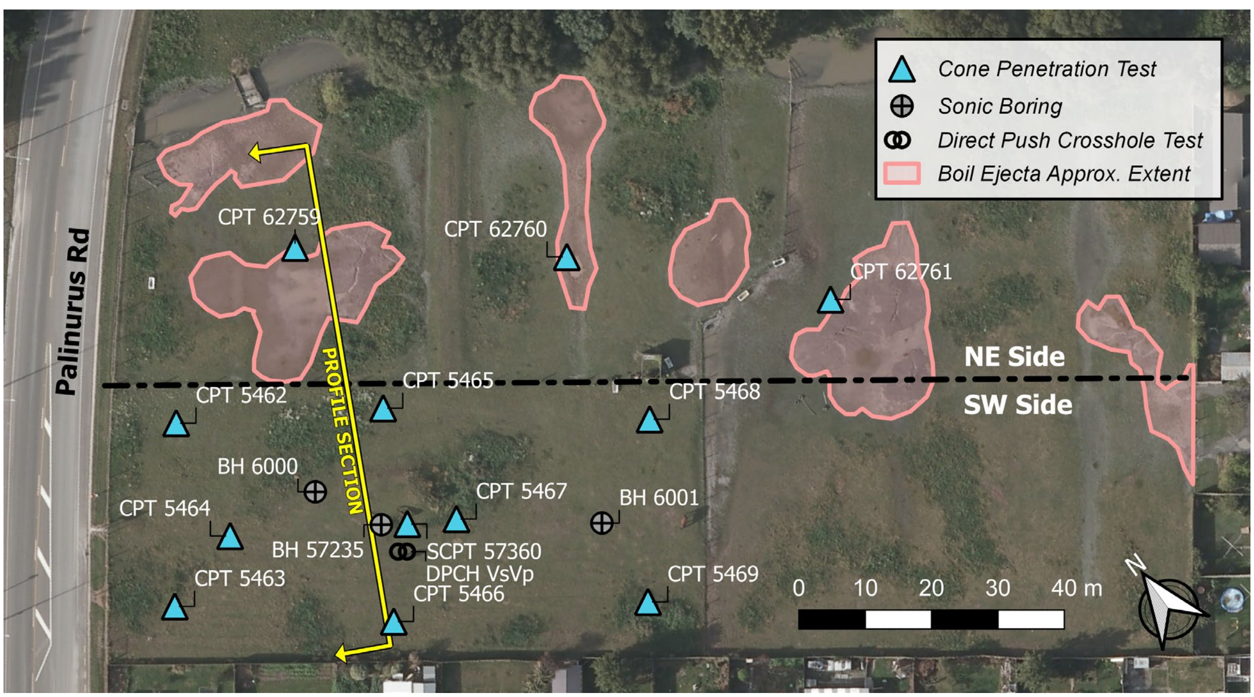

Fig. 2. Palinurus Road site plan with background image taken after the Christchurch earthquake on 24 February 2011 [base imagery from New Zealand Mapping Ltd. (2014); made with QGIS].

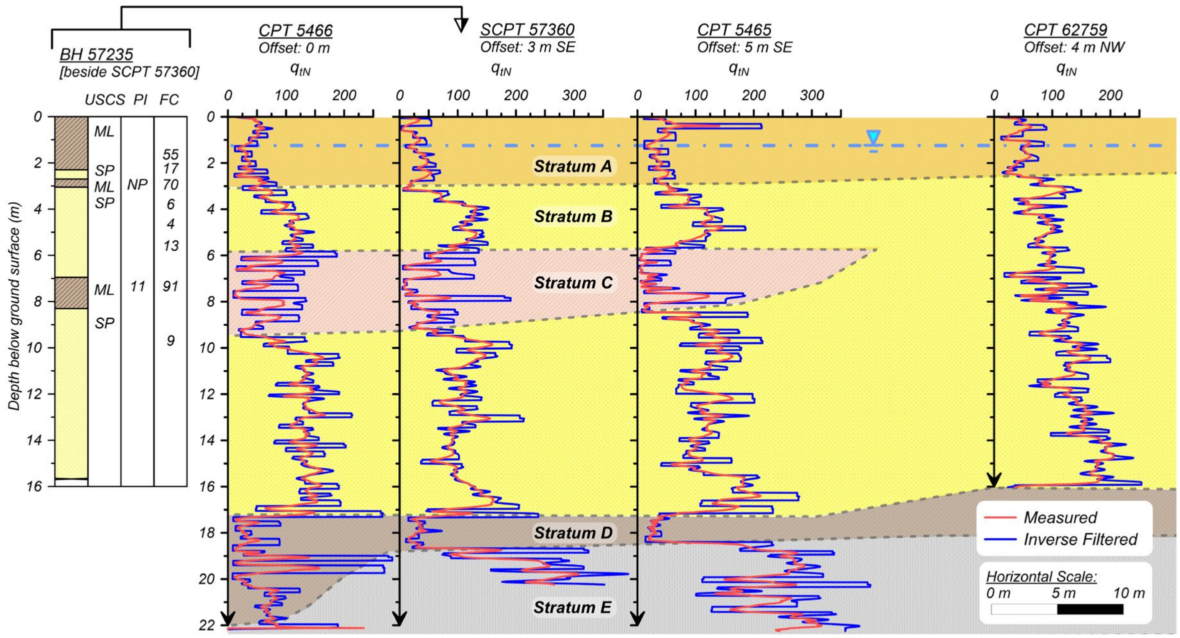

Fig. 3. Palinurus Road interpreted *SW-NE* subsurface profile section with measured and inverse filtered CPT data.

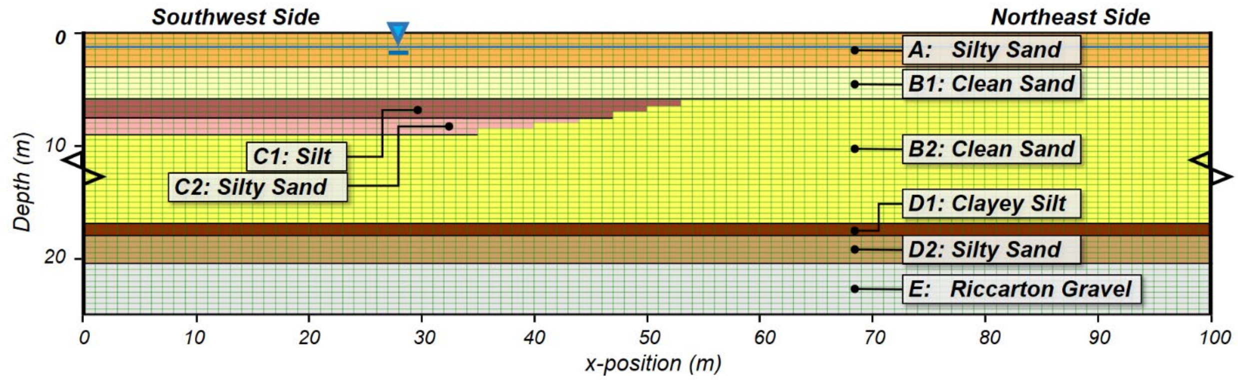

Fig. 4. Central 100-m long segment of the FLAC mesh used for Palinurus Road NDAs.

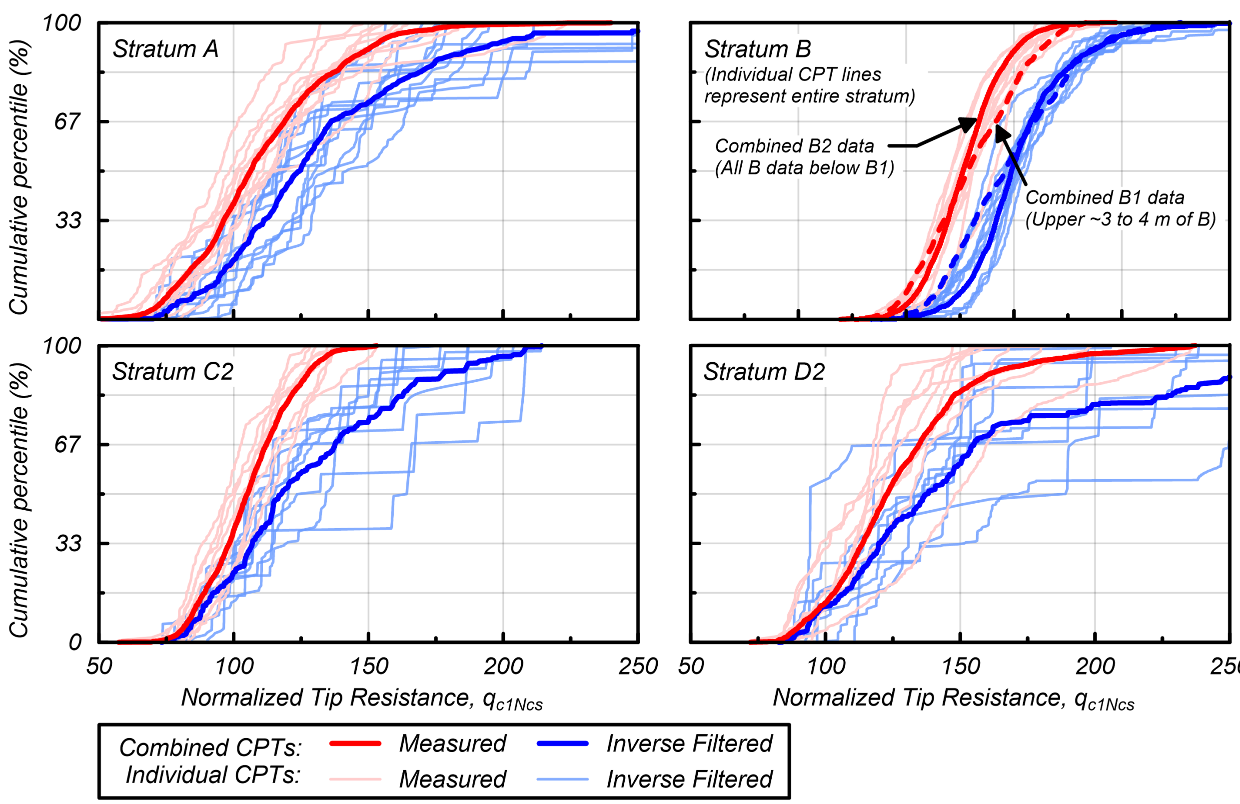

Fig. 5. Cumulative distributions of the measured and inverse filtered normalized clean sand corrected tip resistance (q_{c1Ncs}) from all CPTs at the site, for all NDA strata modeled as PM4Sand.

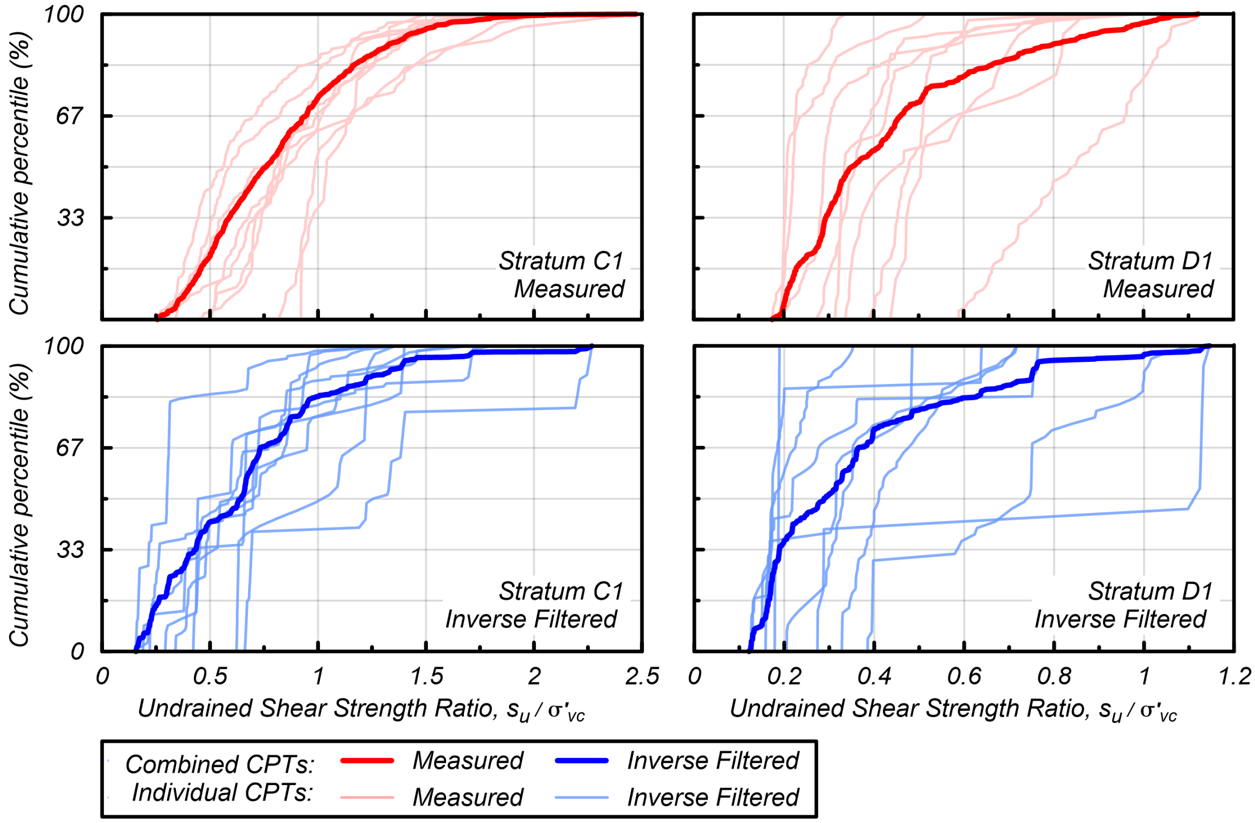

Fig. 6. Cumulative distributions of the measured and inverse filtered the undrained shear strength ratio (s_u/σ'_{vc}) from all CPTs at the site, for all NDA strata modeled as PM4Silt.

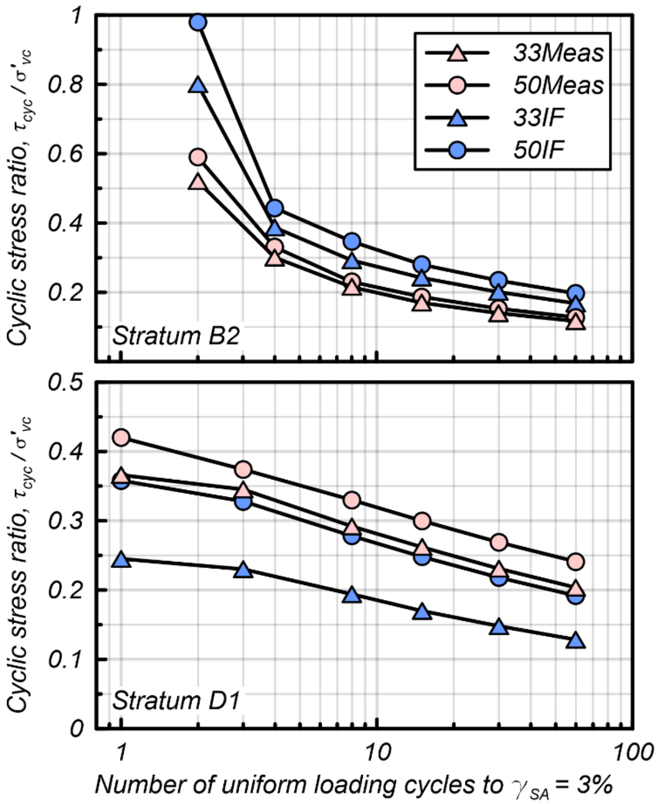

Fig. 7. Minimum CSR to reach 3% single-amplitude shear strain in a given number (N) of stress cycles for four parametric cases: (a) using PM4Sand for stratum B2, and (b) using PM4Silt for stratum D1.

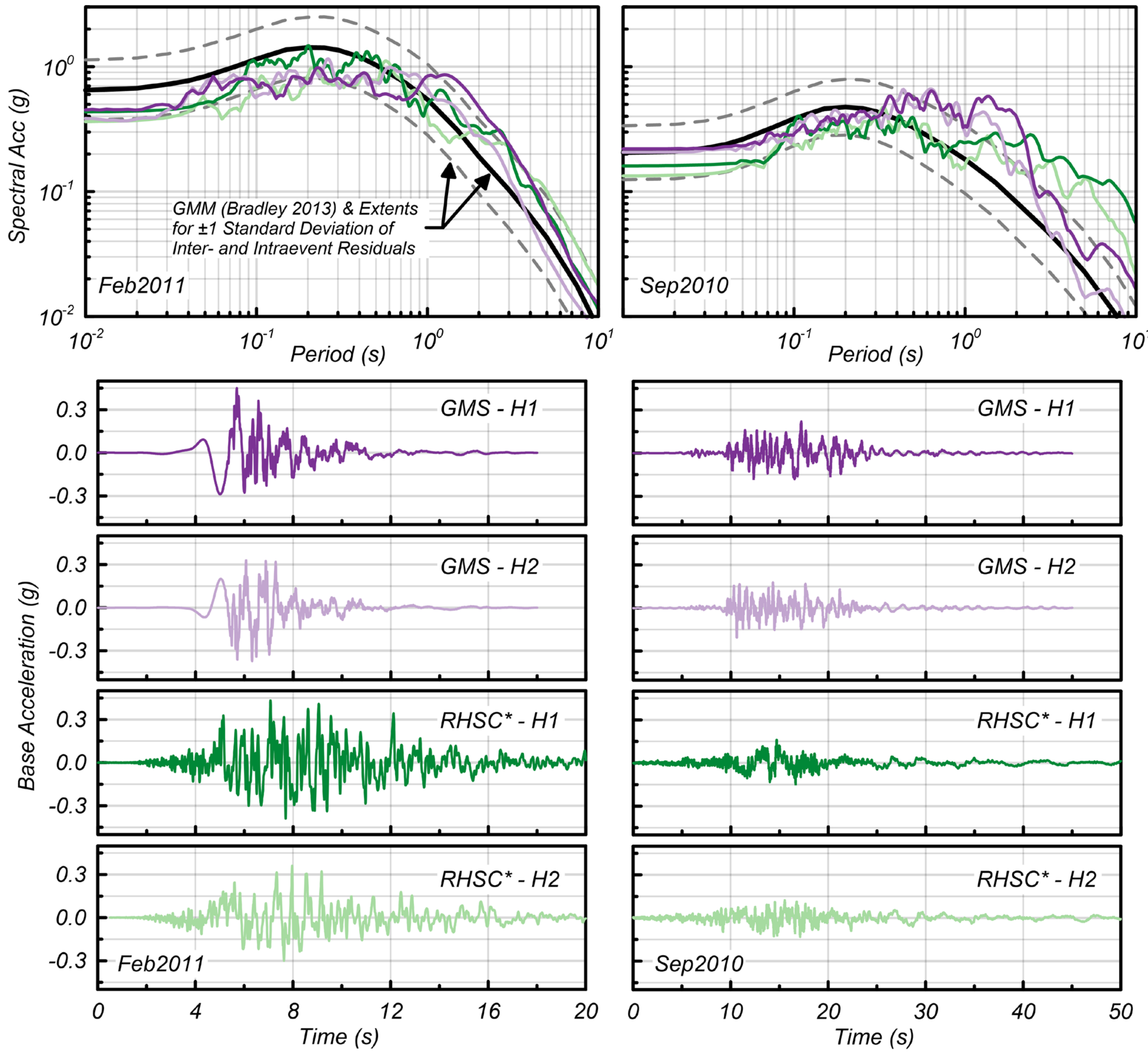

Fig. 8. Acceleration response spectra and time histories of input ground motions considered for NDAs.

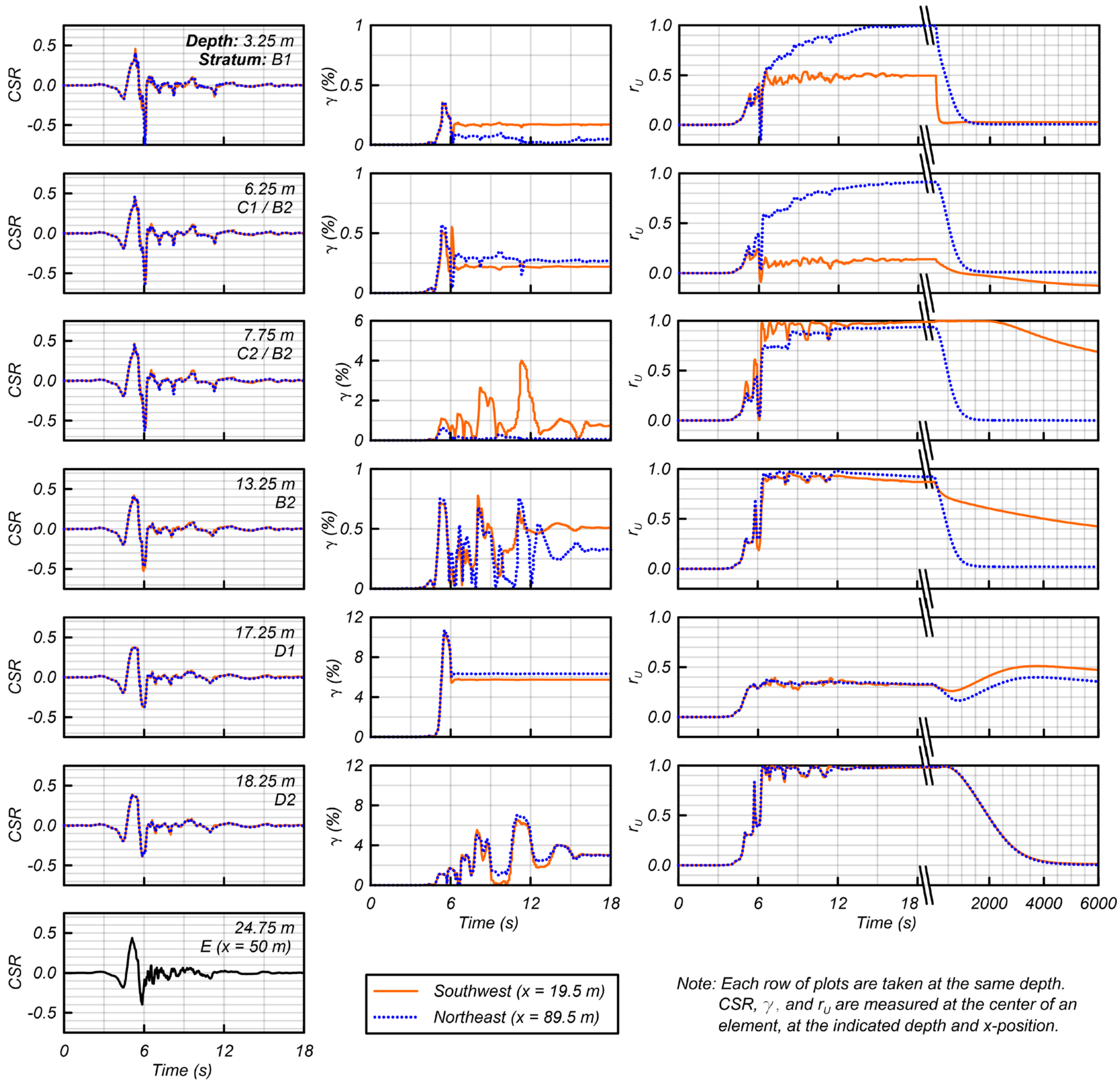

Fig. 9. Time histories from the *33Meas* model with the *Feb2011* GMS-H1 motion.

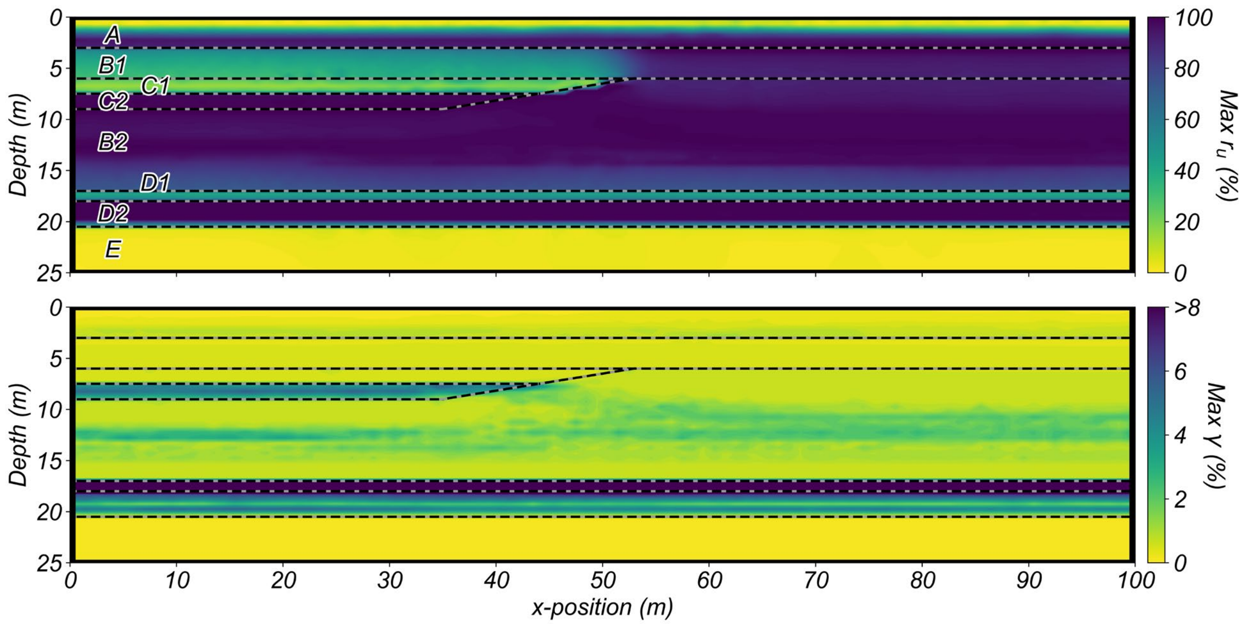

Fig. 10. Contour plots for the *33Meas* model with the *Feb2011* GMS-H1 motion: (a) maximum excess pore pressure ratio, and (b) maximum shear strain.

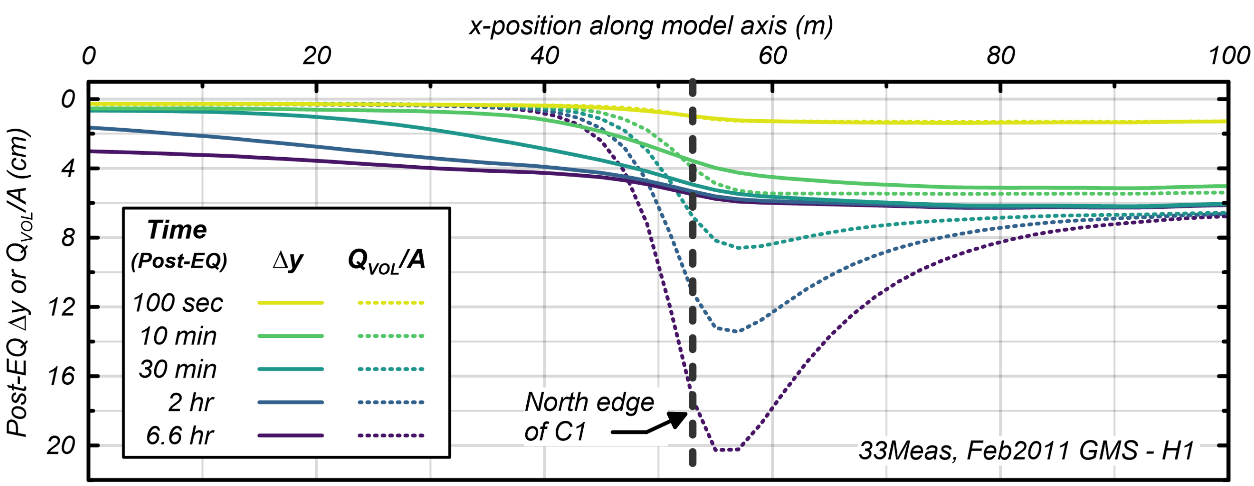

Fig. 11. Isochrones of the total outflow volume per unit area (Q_{VOL}/A) and vertical displacement relative to stratum D1 (Δy) as measured at the phreatic surface for the *33Meas* model with the *Feb2011* GMS-H1 motion.

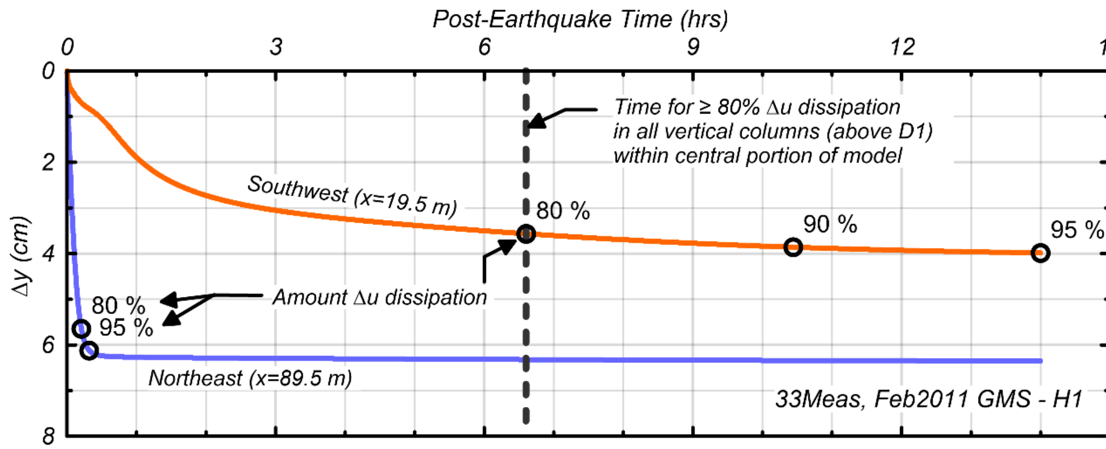

Fig. 12. Time histories of post-earthquake ground surface vertical displacement relative to stratum D1 (Δy) for the 33Meas model with the Feb 2011 GMS-H1 motion.

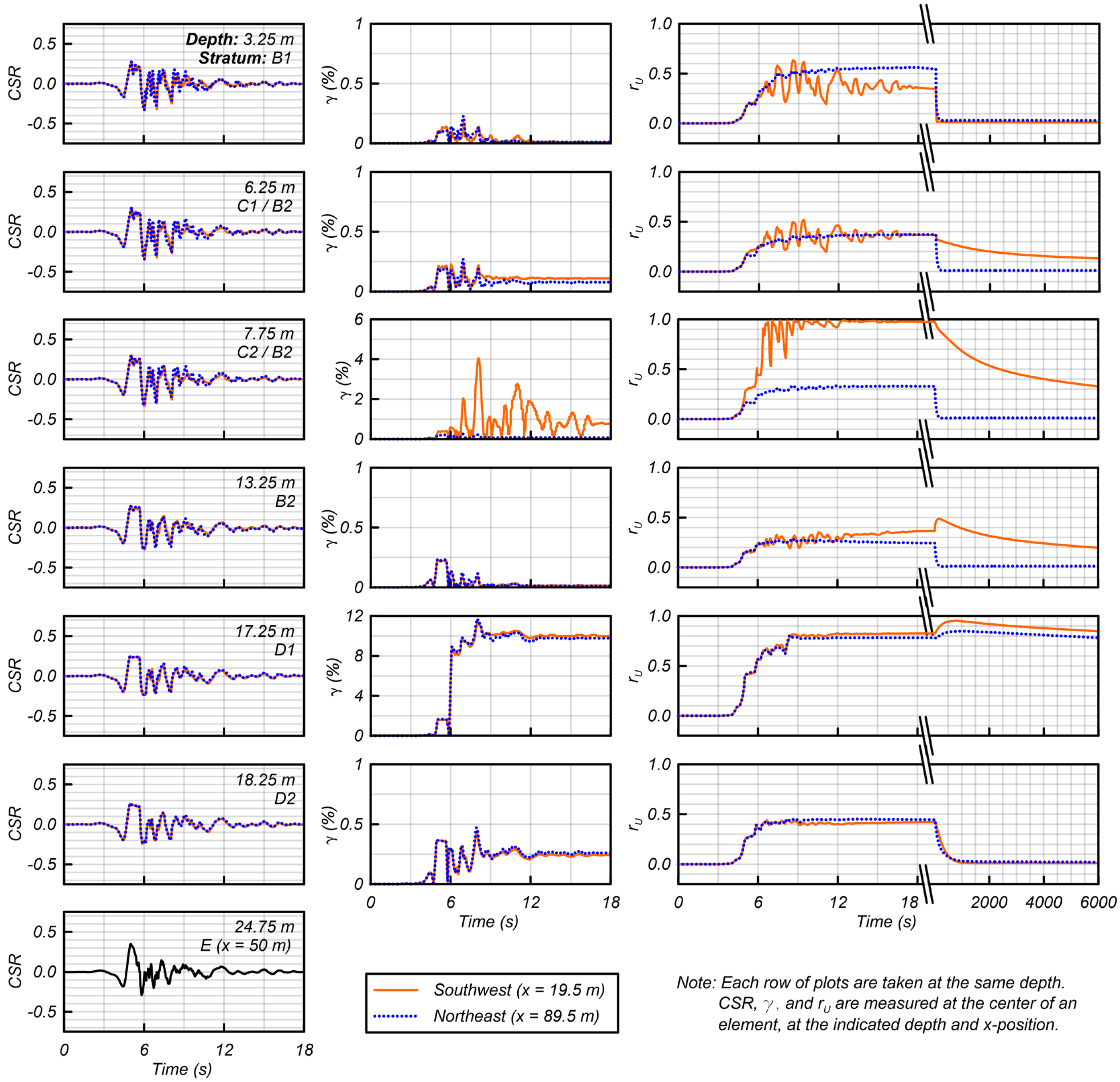

Fig. 13. Time histories from the *33IF* model with the *Feb2011* GMS-H1 motion.

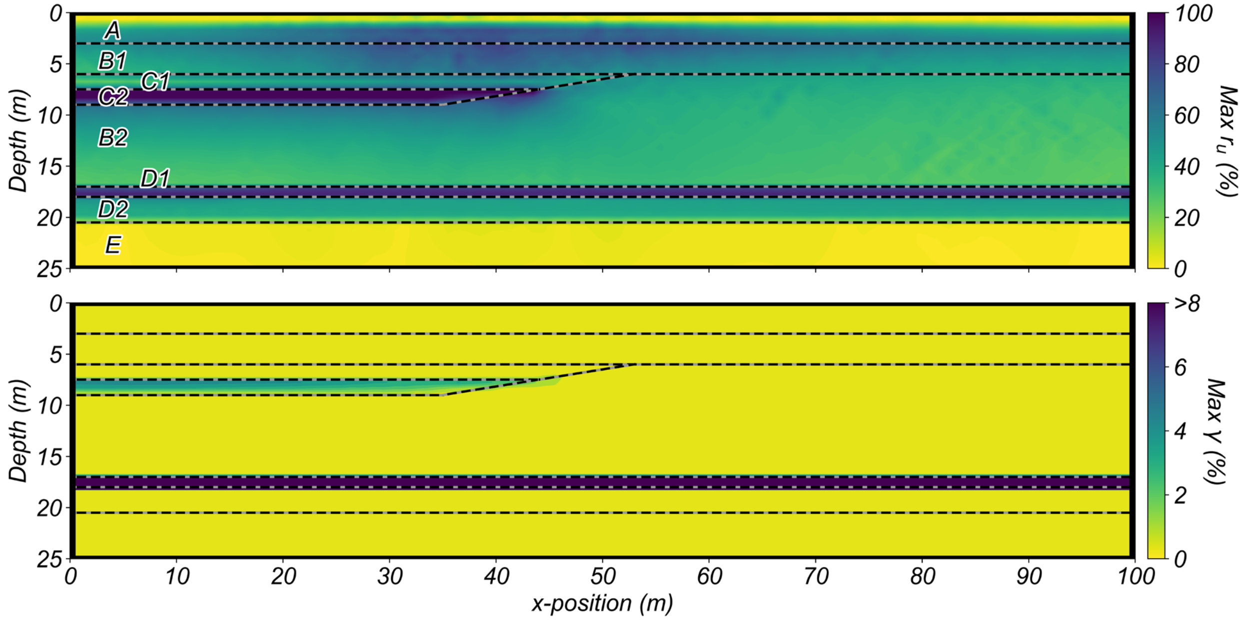

Fig. 14. Contour plots for the *33IF* model with the *Feb2011* GMS-H1 motion*:* (a) maximum excess pore pressure ratio, and (b) maximum shear strain.

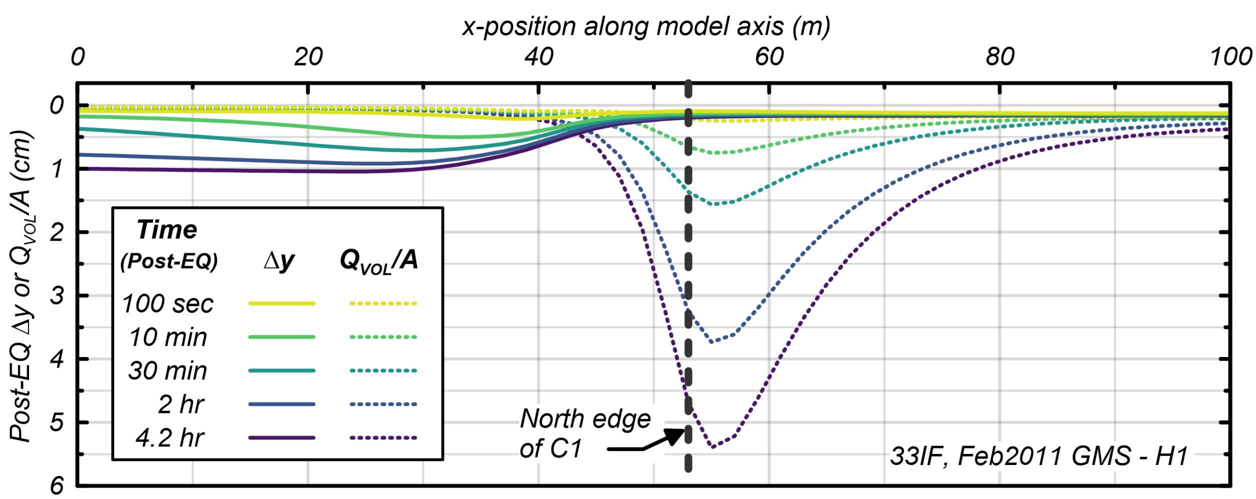

Fig. 15. Isochrones of the total outflow volume per unit area (Q_{VOL}/A) and vertical displacement relative to stratum D1 (Δy) as measured at the phreatic surface for the *33IF* model with the *Feb2011* GMS-H1 motion.

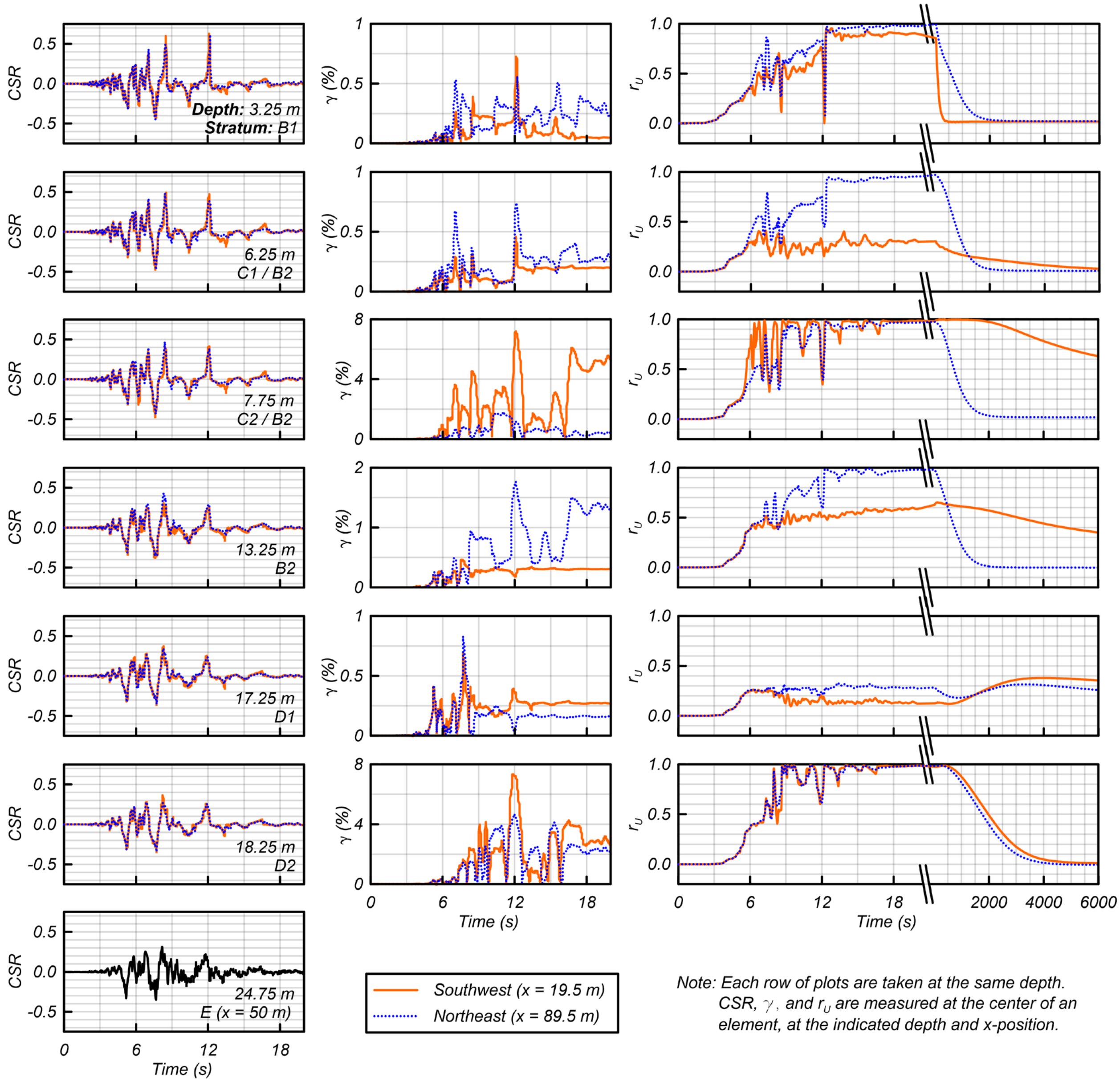

Fig. 16. Time histories from the *33Meas* model with the *Feb2011* RHSC*-H1 motion.

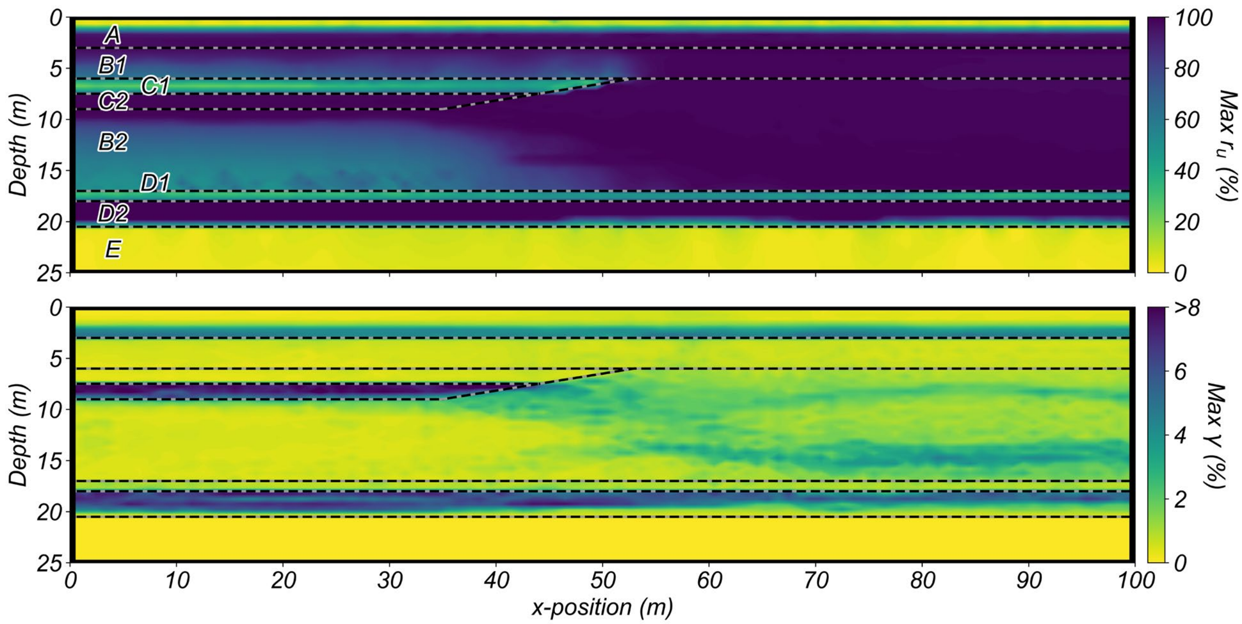

Fig. 17. Contour plots for the *33Meas* model with the *Feb2011* RHSC*-H1 motion: (a) maximum excess pore pressure ratio, and (b) maximum shear strain.

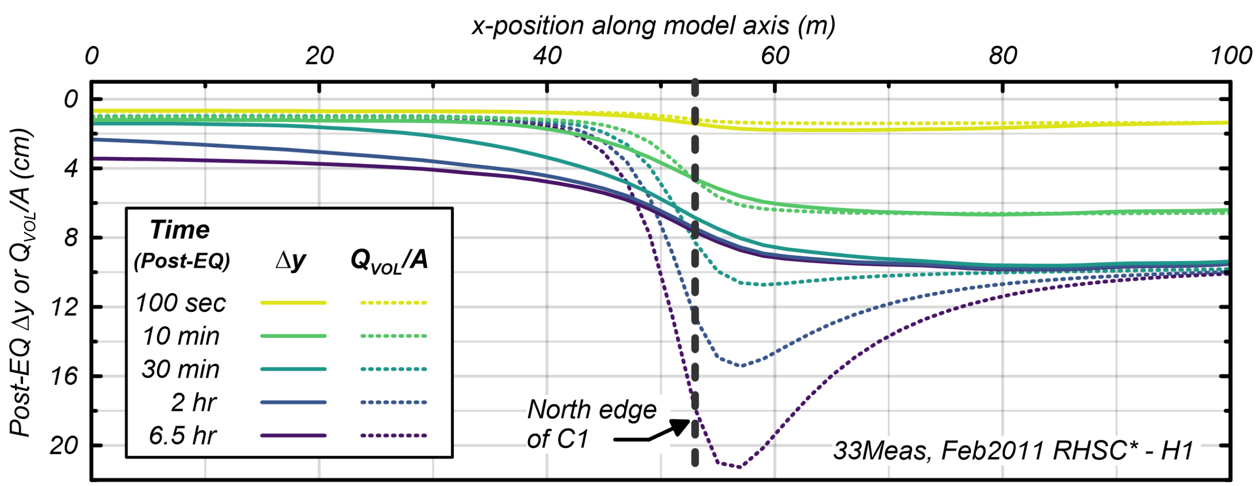

Fig. 18. Isochrones of the total outflow volume per unit area (Q_{VOL}/A) and vertical displacement relative to stratum D1 (Δy) as measured at the phreatic surface for the *33Meas* model with the *Feb2011* RHSC*-H1 motion.

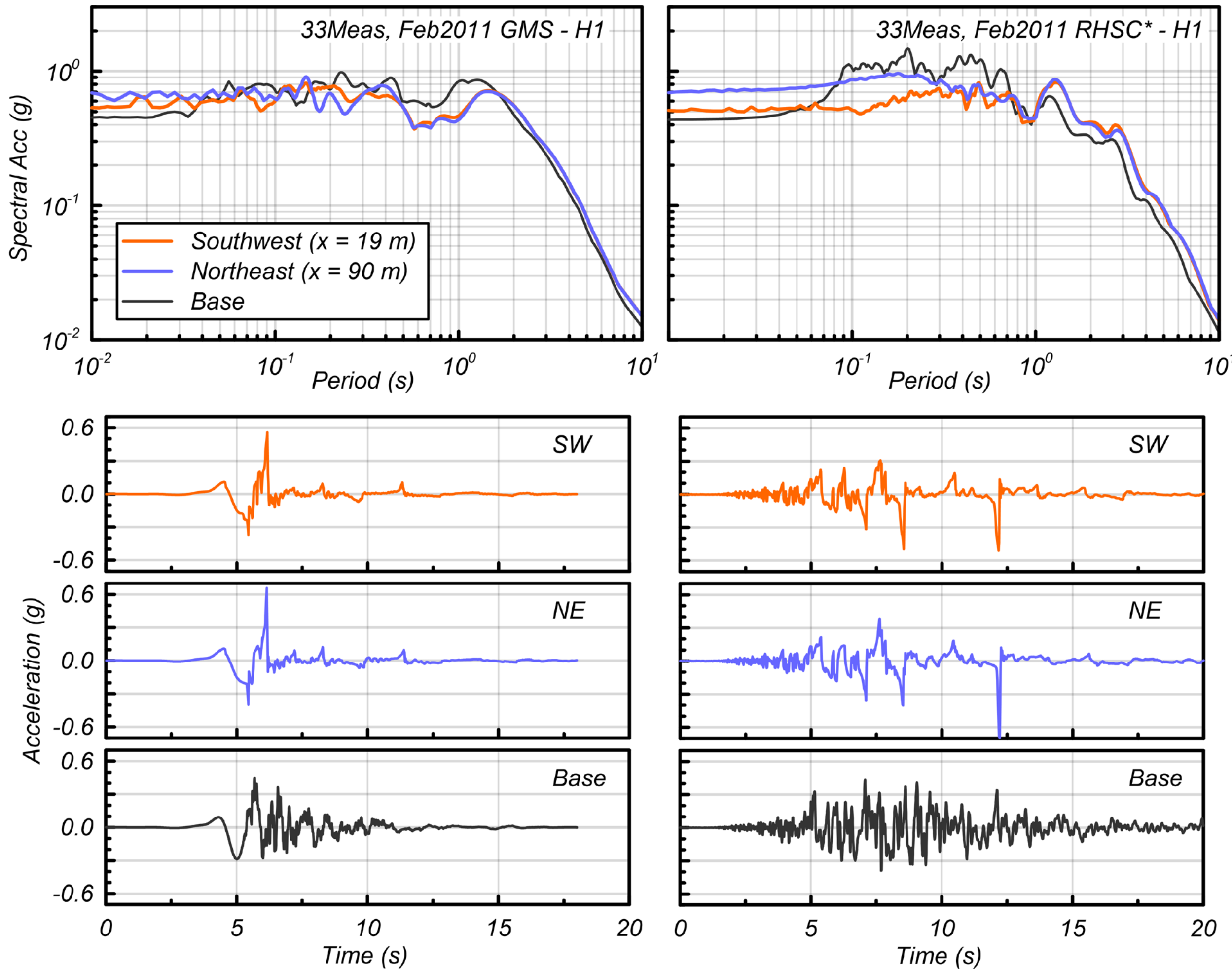

Fig. 19. Comparison of acceleration response spectra and time histories of base input and surface ground motions from the *33Meas* model with the GMS-H1 and RHSC*-H1 motions for the *Feb2011* event.

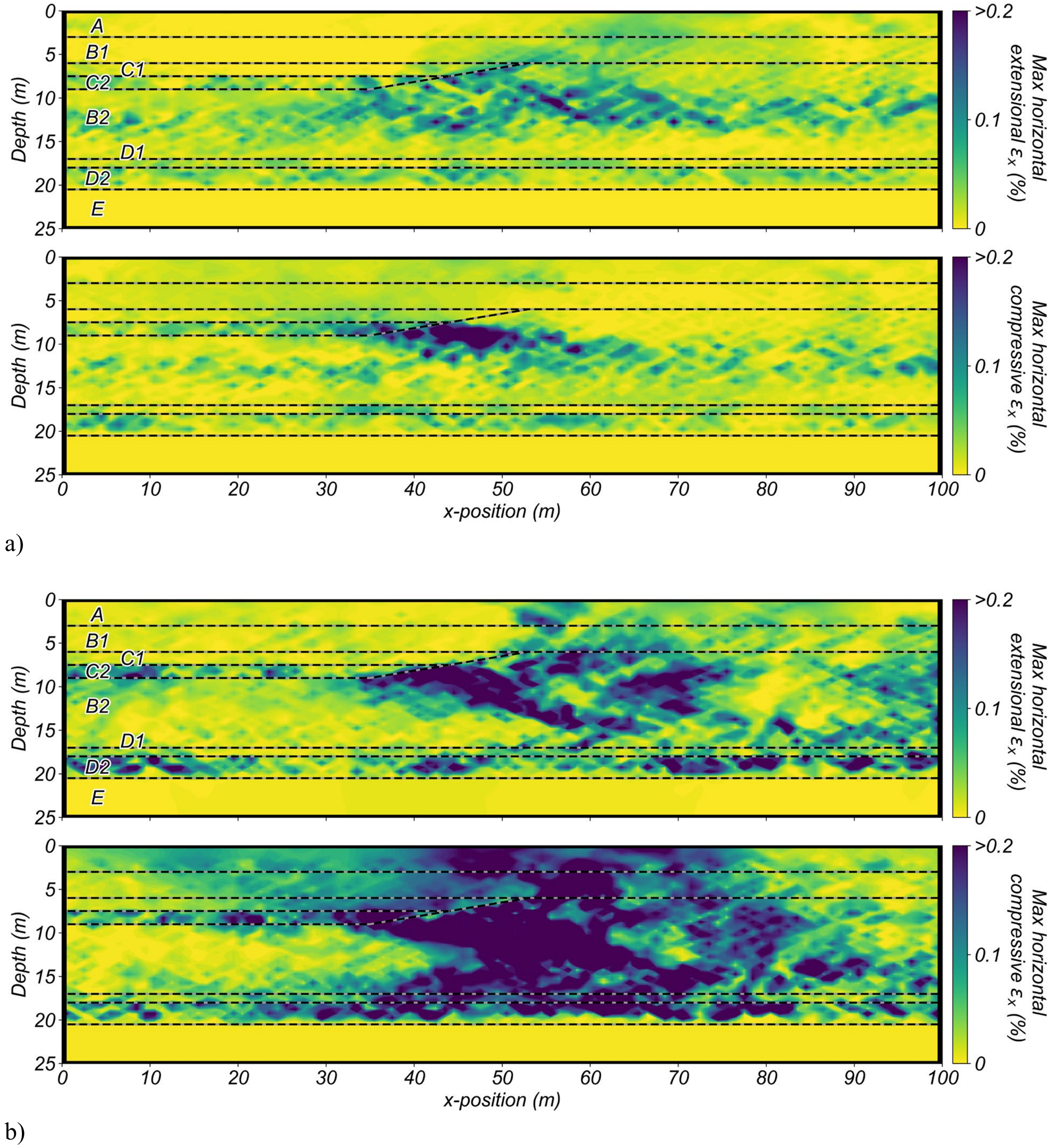

Fig. 20. Contour plots of maximum horizontal extensional and compressive strains for the (a) *33Meas, Feb2011* GMS-H1 (baseline), and (b) *33Meas, Feb2011* RHSC*-H1 NDA models.

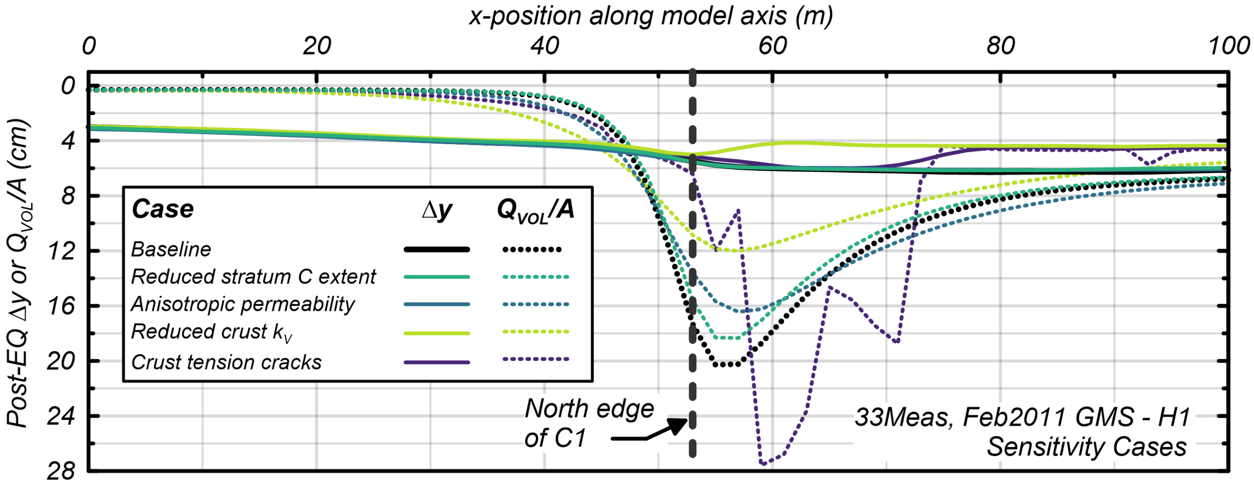

Fig. 21. Total outflow volume per unit area (Q_{VOL}/A) and vertical displacement relative to stratum D1 (Δy) as measured at the phreatic surface, for different NDA model assumptions related to pore pressure diffusion.